Nanofabrication of Functional One-dimensional Mn-based Building Blocks by Chemical Vapor Deposition

Chapter · January 2016

DOI: 10.13140/RG.2.1.2114.7921

3 authors:

Juan Beltran-Huarac
East Carolina University
52 PUBLICATIONS **611** CITATIONS
SEE PROFILE

Brad R. Weiner
University of Puerto Rico at Rio Piedras
222 PUBLICATIONS **2,925** CITATIONS
SEE PROFILE

Gerardo Morell
University of Puerto Rico at Rio Piedras
240 PUBLICATIONS **3,016** CITATIONS
SEE PROFILE

5

Nanofabrication of Functional One - dimensional Mn-based Building Blocks by Chemical Vapor Deposition

Juan Beltran-Huarac*, Brad R. Weiner and Gerardo Morell

Department of Physics, University of Puerto Rico, San Juan, PR 00936, USA
Department of Chemistry, University of Puerto Rico, San Juan, PR 00931, USA
Molecular Sciences Research Center, University of Puerto Rico, San Juan, PR 00926, USA

Outline:

Introduction

Nanostructures exhibiting size-dependent physical, chemical, magnetic and electronic properties, which are substantially distinct from their isolated atoms and molecules, and bulk counterparts, are of great interest to the scientific community. They lie at the border between classical and quantum mechanics. The need of integrating such nanostructures with conventional systems has fostered novel miniaturization strategies, developed and implemented for the design of more-effective devices and smart biological platforms to advance cutting-edge technological innovations in many fields of science. Among the great diversity of nanoscale buildings blocks (BBs), one-dimensional semiconducting nanostructures, including nanowires (NWs), nanotubes (NTs), nanoribbons (NRs) nanobelts (NBs), and nanosaws (NSs) have gained a great deal of attention due to their functional properties and their ability to be used as key elements of devices, interconnects and nano-platforms. They are also used to describe some concerns related to dimensionality, morphology-tuned stability, quantum confinement transport phenomena and transformation mechanisms [1-10]. Their stepwise integration with organic or inorganic hybrid systems facilitates that their properties can be tailored, thus inducing multifunctionality and new cross characteristics, which can be different from their constituents.

Since the discovery of carbon nanotubes (CNTs) by Iijima [11] in 1990, intense investigation has been devoted to the fabrication of these one-dimensional nanostructures, which have resulted in a great variety of methods and techniques capable of producing unique geometrical shapes with different structural phases. Although their confinement effect is along the radial direction, their geometry provides: i) high surface-to-volume ratios, ii) curvature radii at nanoscale, iii) highly stable structure surfaces, iv) large mechanical flexibilities, and v) intriguing anisotropic properties. Moreover, as elements of nanodevices, their length (as long as a few centimeters) is suitable for easier manipulation during the fabrication process. Their electronic and mechanical properties are in general analogous to those of semiconducting and metallic CNTs, which make them more attractive to advanced optoelectronics and field-effect transistors [11]. Similar to semiconducting nanocrystals, the size of 1D nanostructures is equivalent to the wavelength of visible light allowing interaction with light on a nanometric scale, which is vital for sensitive photodetection, Fabry-Perot mode stimulated emission, efficient luminescence, and wave guiding of photons. This aspect has been widely exploited in devices, including photovoltaic cells, light-emitting diodes (LEDs), photodiodes, optical sensors and lasers [1,3]. Furthermore, their absorption, emission and stimulated emission can be tailored by some factors, including the growth direction, doping level, facets, crystal structure, composition, and defect and impurity concentrations. These factors are governed not only by growth processes, but also by the synthetic methodology and experimental design to induce a preferentially oriented growth along a specific axis [9].

Nanostructures that include metal sulfides have been studied over the past few decades due to their capability to induce spontaneous polarization, which results from the stacking configuration of their surface terminations that are ionically charged. They chemical, physical, magnetic, optical and electrical properties can be easily tuned, for instance, controlling their anion deficiency and cation valence state [4]. In this book chapter, we review the most recently advances in nanofabrication, covering the meaningful breakthroughs and relevant findings related to the formation, structure, morphology, properties and technological applications of one-dimensional functional Mn-based BBs (OFMBBs). Special focus is devoted to sulfides and the effect of using metal catalysts (with controlled size, geometry, composition and distribution) during their deposition by chemical vapor deposition. Finally, the facile integration of OFMBBs with graphitic carbon layers and their doping with transition metals are also highlighted.

One-dimensional Functional Mn-based Building Blocks

The quest for smaller functional elements of devices has stimulated increased interest in charge-transfer phenomena at the nanoscale [12]. OFMBBs are particularly appealing given that the excited states of high-spin Mn ions induce unusual *d-d* energy transfer processes, which is critical for better understanding the performance of electron- and spin-based devices. Extensive research focused on sulfide-based polymorphic nano- and micro-structured materials and hierarchical structures have revealed that excited states of Mn ions can generate broad emission bands in the UV-Vis range at room temperature (RT), acting as either constituent elements or impurities within a host material. Recently, the *d-d* energy transfer induced transitions in Mn^{2+} ions have been correlated with the antiferromagnetic spin ordering [12]. Thus, the inclusion of Mn impurities not only induces multifunctionality, but also allows synergistic magneto-optical coupling and other cross properties. The high abundance and low cost of Mn have also fueled exploratory studies on the electrochemical performance of OFMBBs as anode materials for Li-ion battery (LIB) technology. These studies indicate that they exhibit high lithium storage capacity, and enhanced and efficient cyclability and rate capability. Hence, Mn-based electrode materials having a theoretical specific capacity higher than that of graphite bring forth new vistas to advance new alternatives in energy storage and conversion [12]. In this regard, connecting tiny Mn-based LIBs in a parallel circuit would enable high power portable devices, such as power tools and electric devices, and comply with environmental concerns and recycling requirements.

More recently, studies on the electrochemical behavior of cytochrome *c* (cyt. *c*) immobilized on Mn-based nanostructured modified glassy carbon electrodes demonstrate that OFMBBs fabricated via a green route can promote direct electron transfer between the electrode and cyt. *c* [12]. In parallel, OFMBBs have been found to be non-toxic, thus being suitable as alternative T_1-bright probes for magnetic resonance imaging (MRI) in order to prevent cases of nephrogenic system fibrosis in patients, who receive a high doses of certain formulations based on conventional gadolinium chelates [13]. This research field is still in its infancy as compared to superparamagnetic iron oxide based T_2-contrast probes. Efforts to study the metabolism and long-term side effects of new Mn-based materials within a biomedical context are crucial to their future clinical adaptation. Accordingly, the fabrication, development and implementation of OFMBBs are crucial in materials science to bring forth new applications in nanobiotechnology.

Among the most important OFMBBs systems reported, sulfides have received more attention in the area of optoelectronics due to their superb photoluminescent (PL) properties, which are used in visible and infrared optics, LEDs and flat-panel displays. In particular, MnS being a p-type direct semiconductor with a wide band gap (E_g~3.2 eV at RT) has allured increased interest due to its ability to emit visible light efficiently, thus being considered as an eco-friendly light source, which represents an excellent alternative for replacing the conventional phosphors based on expensive, toxic rare earths that are currently employed in LED technology [14]. MnS crystallizes in three structural phases: Rock salt (cubic *α*-MnS), zinc blende (cubic *β*-MnS) and wurtzite (hexagonal *γ*-MnS). Special interest has been devoted on metastable hexagonal *γ*-MnS nanostructures due to their enhanced structural stability and superior optical features [15-18]. For instance, phosphors of MnS self-assembled in the wurtzite phase at temperatures as high as ~1100 K significantly reduce the grain boundary scattering present in cubic MnS, which enables optimization of the photoluminescence response. Bulk *γ*-MnS does not exist in nature, but its synthesis is possible in the laboratory under unusual conditions. *γ*-MnS nanostructures exhibit improved chemical, electrical and magneto-optical properties, when compared to rock-salt MnS [6]. Some methods to grow *γ*-MnS hierarchical structures and microspheres have been reported; however, there are few

reports on the self-assembly of nanostructured *γ*-MnS [19-27]. Jun and co-workers [24] reported the study of the architectural control of MnS nanostructures via thermolysis of nonpyrophoric and less-reactive single molecular precursors using a monosurfactant system. They obtained nanostructures with different shapes (wires, spheres and cubes with low aspect ratios) by varying the growth temperature (see Figure 5.1). They also found that one of the most vital factors to determine the final architecture is the crystalline phase of the initial nuclei and the balanced control between kinetic and thermodynamic growth regimes.

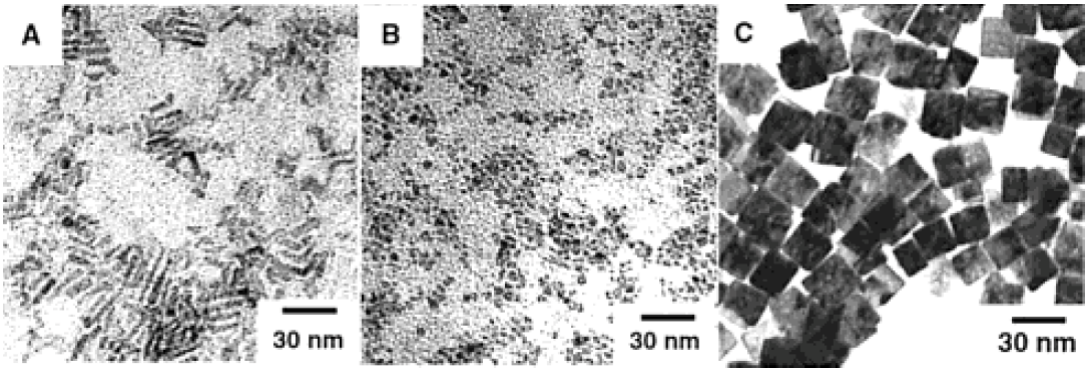

FIGURE 5.1
TEM images of MnS nanostructures with different shapes: (A) wires, (B) spheres and (C) cubes. Copyright © 2002. Reproduced with permission from American Chemical Society

Zhang et al. [25] using anodized an aluminum oxide (AAO) template under hydrothermal conditions obtained a high-density aligned MnS nanorods with a narrow length distribution (see Figure 5.2). The authors also found that the porous surface of the AAO template and the precursor concentrations play key roles in the nucleation stage of such highly-oriented nanostructures. Ge and Li [26] obtained single-crystal MnS NWs with different diameters via a controllable chemical vapor deposition (CVD) process at high temperatures (>1050 K), as depicted in Figure 5.3. They found that the nanowire synthesis is governed by the vapor-solid (VS) mechanism, and that the growth axis of the nanowires is related to their crystallographic characteristics. In this study, the temperature during the synthetic procedure was determinant to control not only the shape but also the crystallinity of the NWs. The authors concluded that this method is expected to be applicable to the synthesis of other metal sulfide semiconductor nanowires. Nonetheless, the wurtzite-structured one-dimensional MnS materials synthesized to date are fragile when exposed to harsh environments, which generate oxidation, deformation, corrosion and contamination given that MnS is highly reactive [28]. In this respect, increased efforts have been made to deposit a protective shell around the core MnS, thus avoiding the formation of any amorphous phase.

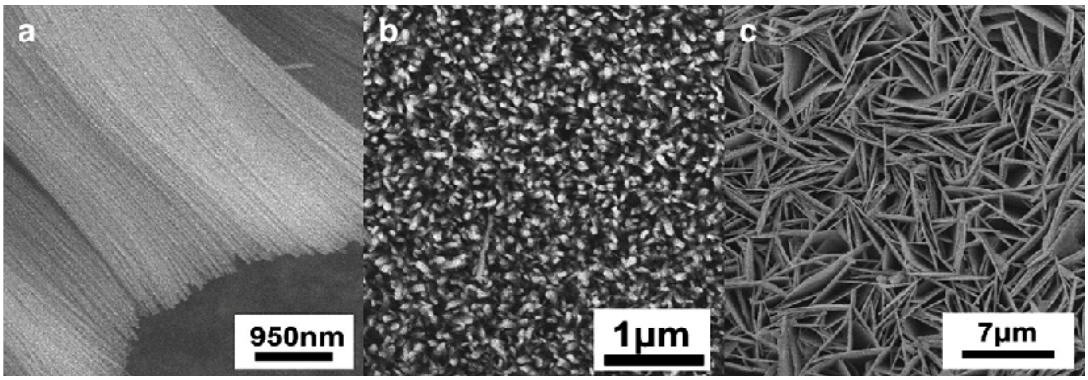

FIGURE 5.2
FE-SEM images of MnS NRs on OAA template using different precursor concentrations in the reaction solution: (a) 2 mol/L, (b) 1 mol/L and (c) 0.05 mol/L. Copyright © 2008. Reproduced with permission from Elsevier

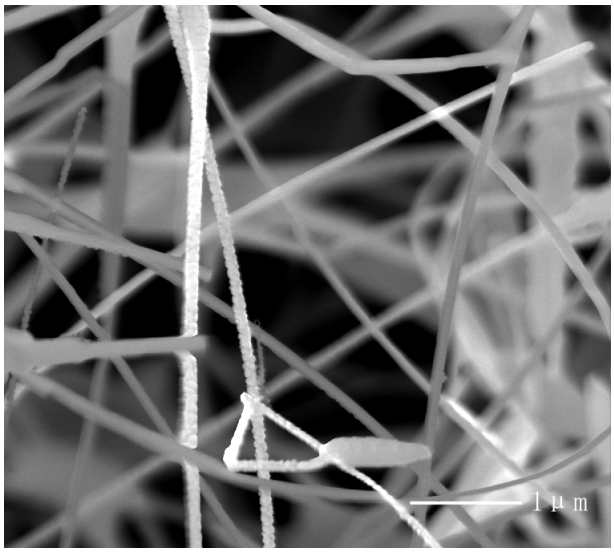

FIGURE 5.3
SEM images of single-crystal MnS NWs synthesized through a simple CVD process. Copyright © 2003. Reproduced with permission from Royal Society of chemistry

Core/shell Systems of OFBBs

Over the past few decades, core/shell 1D systems have been used to encapsulate reactive core materials, such as MnS, within different shell materials in order to generate a physical barrier between the interior and the surrounding medium. This enables core materials to be less sensitive to environmental changes, surface chemistry and photo-oxidation, providing enhanced stability and more efficient surface passivation. The purpose of the protective shell is not only to isolate the core but also to endow single-component 1D compounds with additional multiple functionalities and

promote synergistic effects [29]. Special interest has been devoted to the nano-encapsulation of cores composed of sulfides, phosphates and intermetallic compounds using CNT layers. The carbon coating prevents material damage from harsh environmental attack, enhances the physical and chemical properties, and acts as a reactive site for nanofabrication of new hybrid materials. In order to prevent the oxidation and decomposition of zinc sulfide (ZnS) NWs, Shen and co-workers [28] employed the thermal evaporation of a mixture of ZnS and SnS powders in a graphite-based crucible to deposit graphitic carbon shells onto single-crystal ZnS NWs. Through this two-stage temperature-controlled tube-furnace CVD method, Shen and co-workers obtained core/shell NWs with high aspect ratios, *i.e.*, diameters of 50-120 nm and lengths of several tens of micrometers, and with outer carbon shells having a thickness of ~2 nm (see Figure 5.4). The coating and allotrope of carbon were confirmed using electron energy loss spectroscopy (EELS), as shown in Figure 5.4. The formation of ZnS/C nanocomposites was explained in terms of the vapor-liquid-solid (VLS) mechanism. The shell not only prevents the oxidation and decomposition of the inner ZnS NWs but also passivates their surface allowing that remaining PL emission coming from the core to be detected. Jeong et al. [30], motivated to employ single-crystal apatite NWs as scaffold materials in orthopedics, graphitized the apatite's surface using gaseous aromatic precursors via a one-step CVD process. Vertically-aligned single-crystal apatite NWs sheathed in graphitic carbon (SANGs) of ~5 μ m length and ~15 nm wide grew along the entire length of an amorphous calcium-rich glass fiber, as shown in Figure 5.5. The authors found that the hexagonal-structured core was surrounded by discontinuous graphitic layers of ~2 nm thick. They demonstrated the presence of elemental Ca, P, C and O in the core, and only elemental C in the shell by means of energy-dispersive X-ray spectroscopy (EDS). In parallel, they detected the C-K shell ionization shell on the periphery of individual SANGs, and the P-$L_{2,3}$, C-K, Ca-$L_{2,3}$ and O-K transitions at the center via EELS.

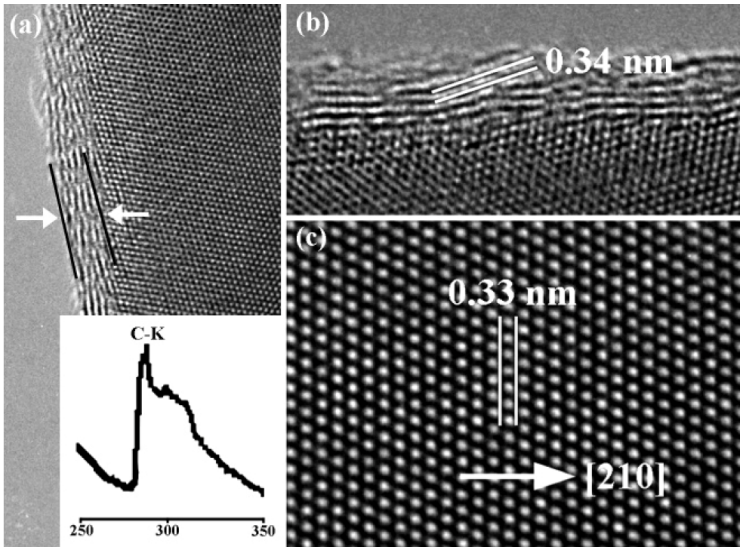

FIGURE 5.4
(a-c) HRTEM images of carbon-coated single-crystal ZnS NWs grown via tube-furnace CVD process. Inset in (a) shows the EELS spectrum of ZnS/C NWs. Copyright © 2006. Reproduced with permission from American Chemical Society

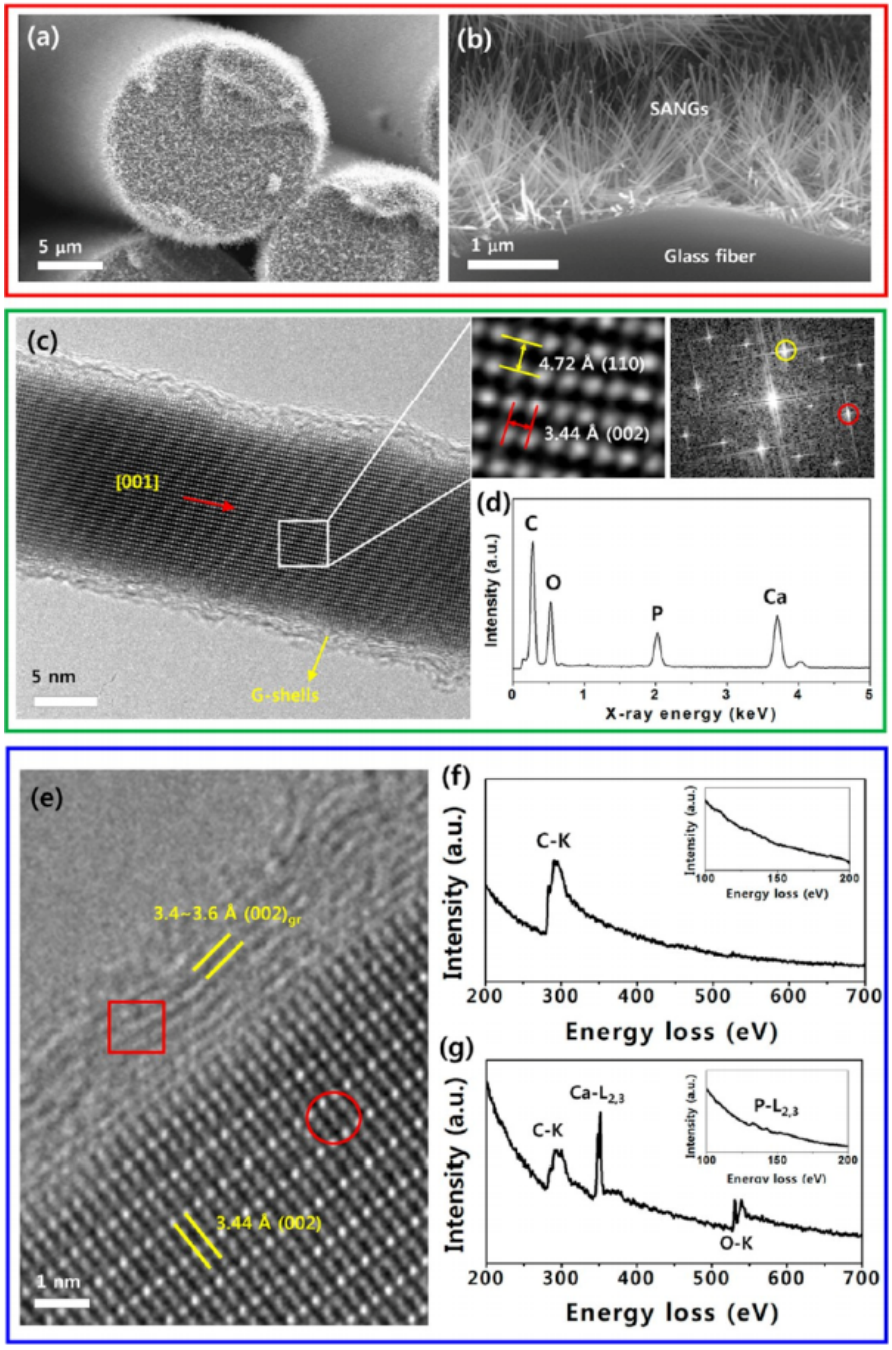

FIGURE 5.5
(a,b) SEM and (c,e) TEM images, (d) EDS spectrum, and EELS spectra at (f) periphery and (g) center of vertically-aligned single-crystal apatite NWs sheathed in graphitic shells . Copyright © 2013. Reproduced with permission from American Chemical Society

The ability of carbon to shield the apatite NWs was then used for osteogenic differentiation in human mesenchymal stem cells, resulting in that they can reflect the dynamic nature of many biological processes, which is needed in tissue engineering. The same research group [31] also reported a simple and reproducible one-step CVD method to fabricate crystalline and superconducting In-Sn intermetallic NWs sheathed in CNTs (see Figure 5.6). The method based on the catalytic reaction of C_2H_2 over a mixture of both SnO_2 and In_2O_3 particles enables the selective synthesis of tetragonal β-In_3Sn, and hexagonal γ-$InSn_4$ NWs with diameters <100 nm and at different SnO_2 to In_2O_3 weight ratios. The authors achieved shells as narrow as 10 nm with well-defined interface zones. They also investigated the nanowire formation parameterizing the time and temperature, and found that the formation of $In_{1-x}Sn_x$ liquid droplets and their infiltration into CNTS are primarily responsible for the growth mechanism of the core–shell nanowires. They concluded that this approach can be extended to the fabrication of analogous binary and ternary one-dimensional nanostructures, which are sensitive to oxidation, with an effective protective shell. Thermolysis, template-assisted hydrothermal process, thermal evaporation and CVD methods are therefore conventional techniques to nanofabricate OFMBBs and one-dimensional core/shell nanostructures that consist of a core material with highly-reactive outer surfaces, and a shell material with sp^2-bonded carbon layers.

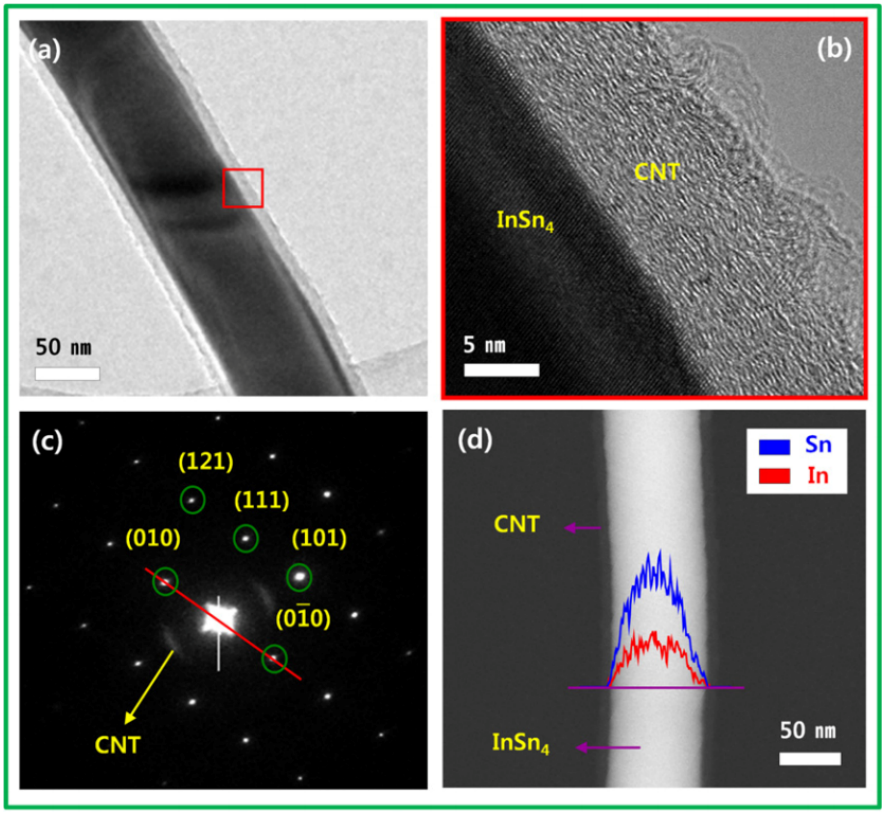

FIGURE 5.6
(a,b) TEM images, (c) selected area electron diffraction (SAED) pattern, and line-scanned elemental mapping profile of core/shell InSn4/CNT NWs grown through a one-step catalytic CVD process. Copyright © 2012. Reproduced with permission from IOP Publishing

An extrapolation of these methods would facilitate the synthesis of OFMBBs coated with carbon via single-step routes. We describe in some detail the most common bottom-up methods used to synthesize OFMBBs in the following section.

Bottom-up Methods to the Synthesis of OFMBBs

The bottom-up approaches to synthesize OFMBBs arose from the need to fabricate devices beyond the capabilities of standard lithography, which conventionally employs top-down approaches [32]. This complementary approach relies on the fabrication of nanoscale devices using one-dimensional nanostructures as building blocks. Whereas in top-down approaches the elements and electronic circuitry are fabricated from a bulk wafer, in bottom-up approaches the structures are assembled from their sub-constituents in an additive manner [33]. Long et al. [34] have reviewed the two main bottom-up strategies for the assembly of OFBB devices that exist. The first one is based on the transfer and alignment of pre-grown OFBBs onto a desired substrate. Examples include assembly by: i) surface chemical binding or electrostatic interactions, ii) microprobes or optical tweezers, iii) microfluidic and microchannels, iv) Langmuir-Blodgett technique, v) blown bubble films, vi) contact or roll printing, vii) dielectrophoresis or electric fields, and viii) magnetic fields [34]. The second strategy consists in the direct growth of aligned OFBBs or nanofibers onto a desired substrate at a specified location. Examples of this type of strategy are: i) direct growth of vertical OFBB arrays, ii) planar growth OFBBs, and assembly by iii) bridging method and iv) electrospinning [34]. Regarding the growth of OFMBBs, the most common bottom-up approaches that are used for this purpose are the VLS, template-assisted electrochemical route and solution-based growth method. The VLS growth mechanism, elucidated by Wagner and Ellis [35] in the 1960s for the first time, has become the most used technique to grow inorganic OFMBBs [36]. In this section we cover the two principal methods, CVD and thermal deposition, to fabricate OFMBBs, whose mechanisms phenomena are largely governed by the metal-catalyst-assisted VLS and VS.

Chemical vapor deposition

CVD involves complex physicochemical processes that lead to depositing ordered crystals onto desired substrates, which result from either chemical reactions of precursor gaseous species or heterogeneous surface reactions. The ability to perform conformal coating distinguishes it from physical vapor deposition, such as sputtering and sublimation processes [37]. In a typical procedure, the precursor gases (including Ar or N_2 inert gases that act as diluent/carrying gases) are delivered into a reaction chamber under specific conditions (temperature and pressure are the most critical parameters), where they come into contact with a heated substrate reacting to form a solid layer of product on the substrate surface. A description of the sequential physical and chemical steps occurring during a CVD process is summarized in Figure 5.7. These steps are: (1) the mass transport of reactant gaseous species to the vicinity of the desired substrate; (2) the diffusion of reactant species through the boundary layer to the substrate surface and/or the homogeneous reactions to form intermediates; (3) the adsorption of reactant species or intermediates on the substrate surface; (4) the surface migration, heterogeneous reaction, inclusion of coating atoms into the growing surface, and formation of by-product species; (5) the desorption of by-products species from the surface reaction; (6) the diffusion of by-product species to the bulk gas; and (7) the transport of by-product gaseous species away from the substrate [37]. We will discuss some aspects in more detail of two CVD systems, which are used to synthesize OFMBBs and OFMBB-

based core/shell systems, and related nanocomposites. The first one is an eco-friendly and cost-effective method carried out within a horizontal tube furnace and with a potential for large-scale production, and the second one is a the low-cost, simple, scalable, and versatile method conducted in a CVD reactor at high temperatures and pressures assisted by a hot filament.

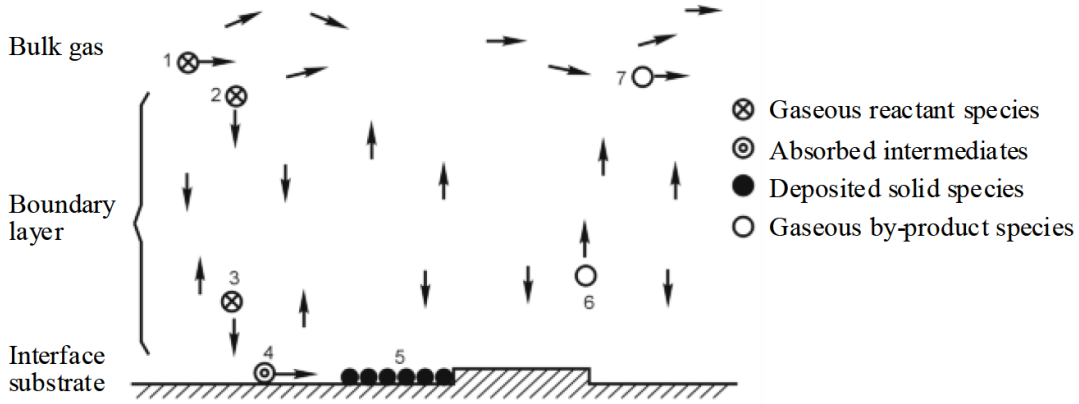

FIGURE 5.7
Schematics of a typical CVD process. Copyright © 2014. Reproduced with permission from ProQuest LLC

Horizontal Tube Furnace

A hot-wall horizontal tube furnace consists of a reaction tube made of fused quartz (Alumina or Pyrex) and an electric heating device with one rotary pump system coupled with a gas supply and a control system. The configuration of the furnace consists of a cylindrical cavity enclosed by heating coils that are embedded in a thermally insulated matrix [38]. The temperature is monitored and controlled by standard thermocouples placed in the middle part of the furnace interfaced to a computer to permit programmed ramping, soaking and sintering (see the upper part of Figure 5.8). A view window is set up at the gas input end of the tube to monitor the growth process, and the output end is connected to a rotary vacuum pump (*ca*. 10-20 mtorr). Both ends are typically sealed by Viton O-rings [39]. In a typical solid-vapor process (thermal evaporation), the carrying/precursor gases are flowed over the condensed or powder source materials and substrates, loaded on boats (preferentially made of alumina) and positioned (taking their melting points into consideration) within the reaction tube. As the temperature is raised, the source materials are vaporized, transported, and condensed to form the desired product (see the lower part of Figure 5.8). The processing parameters (*e.g*. temperature, pressure, environment, substrate, carrying gases, flow rates and evaporation time periods) can be optimized empirically, leading to high-quality products grown on the mother substrates. The source temperature choice (lower than the melting point) is directly related to the degree of volatility of the source materials. Likewise, the pressure is established according to the evaporation rate or vapor pressure of the source materials [39,40]. The substrate temperature often rises by decreasing the distance from the position of the source materials. In this type of system, oxygen contamination (from surface oxides and relatively low vacuum) as a result of the thermal evaporation process is unavoidable.

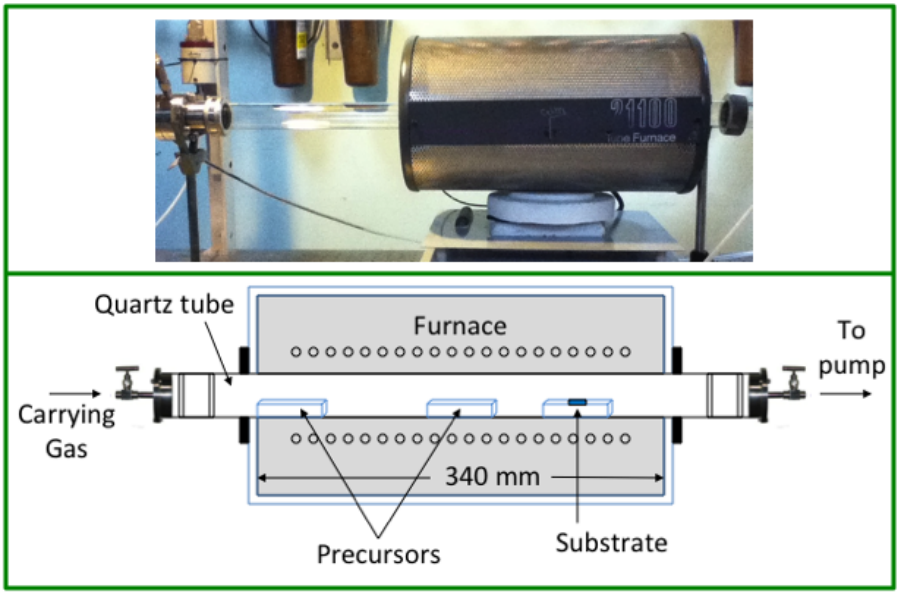

FIGURE 5.8
Optical image of a hot-wall horizontal tube furnace (upper) and its corresponding transverse section (lower) for a typical experiment

However, the concentration of oxygen species can be flushed out by increasing the level of vacuum and generating denser starting vapor concentrations in the active zone. This is a critical issue given that oxygen can influence not only the volatility of the source materials and their corresponding stoichiometry (vapor phase), but also the formation, quality and purity of the final products. Lastly, the growth time and the length of inputting the carrier gas must be known for specific experiments since the growth kinetics can be significantly affected by a slight modification of either one or both.

Hot Filament CVD

The hot filament-assisted CVD (HFCVD) system, developed by Matsumoto and co-workers [41] comprises a cylindrical chamber, wherein all the physicochemical complex reactions occur during the deposition process (see Figure 5.9 adapted from reference [42]). This technique offers uniform and conformal coverage of large areas of uneven or structured surfaces, and is simpler and more flexible in the tuning of the film composition when compared to physical vapor deposition [43]. Also, it can be used to grow high-quality OFMBBs. The typical filament (tungsten, tantalum or iridium) temperatures are in the range of 1700-1800 °C (depending on material deposited and metal-organic precursors). The hot filaments are used to fully decompose the precursors and evacuate the formed radicals from the filament itself towards the substrate [43]. A coiled filament is coupled with an electrical feedthrough, which is attached to a manipulator positioned approximately a few centimeters above the substrate, wherein the film deposition is led from highly active species. The resulting vapor mixture from evaporation of precursors under vacuum is transported by the carrier gas (commonly argon) into the active zone of the substrate, passing through the hot filament spirals. This process leads to the film formation on the cooler substrate.

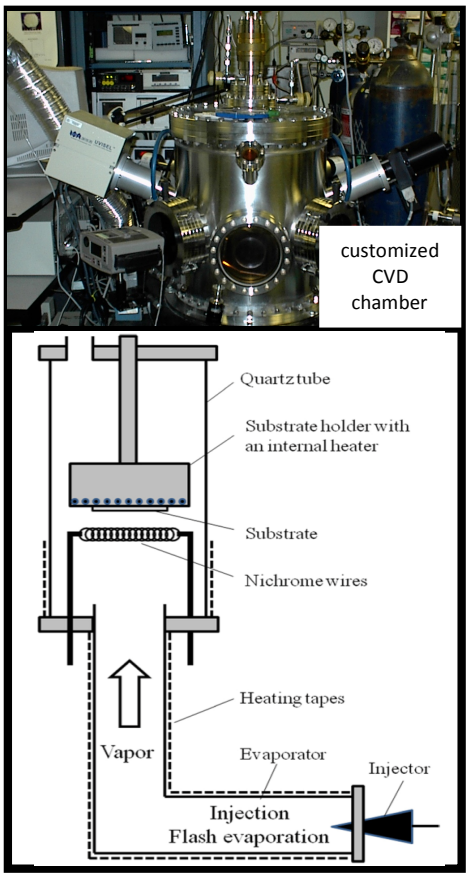

FIGURE 5.9
Optical image (upper) and transverse section (lower) of a HFCVD reactor used for a typical experiment.

In oxides, it has been reported that the use of a pulsed liquid injection system and a single solution of mixed precursors, deliver great flexibility to change the growth rates and film composition by varying the time and frequency of the pulses, and the composition and concentration of the solution [43]. Such a solution of precursors is injected into an evaporator heated at 200 °C at a frequency of 2 Hz, a pulse time of 3 ms, and a dose mass of ~3 mg [43]. Abrutis and co-workers reported growth rates increased by a factor of ~10-20, when compared to traditional CVD conditions, to deposit zinc oxide [43]. The carrier gas flow (Ar + O_2) was set at 250 sccm, with an O_2 content of 20% and total pressure of 1.33 kPa, achieving films as thick as ~160 nm.
The HFCVD process is thus versatile, simple and low-cost and offers the ease of scale-up to large deposition areas and high growth rates. Although the filament of a HFCVD system sometimes contaminates (inherent impurities) the growing samples and its lifetime is limited (due to the resistance of the filament), this technique enables the deposition of high-quality OFMBBs on the surface of any desired (seeded) substrate by adjusting the window of experimental parameters.

Thermal evaporation

Among the physical vapor deposition techniques, thermal evaporation is one of most common routes used to grow one-dimensional single-crystal uniform semiconducting, metallic and metal-oxide materials [40]. The driving forces and the intrinsic advantages of this non-directional deposition method lies in its cost effective volume production and reproducibility [44]. The processes that involve the vaporization at high temperatures of condensed or powder source materials (located in the bottom of the chamber) or the utilization of precursor gases to form (fixing the temperature, pressure, atmosphere, catalyst and substrate) the desired products, are usually conducted within a horizontal tube furnace, HFCVD reactor or vacuum vessel (see Figure 5.10). The heating source is generally an electron beam, but filament evaporation is also used. The chamber is typically pumped to 10^{-6} torr background pressure. During deposition, the distance between the source and the substrate is set at tens of centimeters, falling within the scale for the required mean free path. The ballistic propagation of the vapor requires a residual gas background below 10^{-5} torr [44]. To control the film composition, the evaporation rates have to be monitored using sensor heads, whereas the feedback loops to the sources serve to stabilize the evaporation rates.

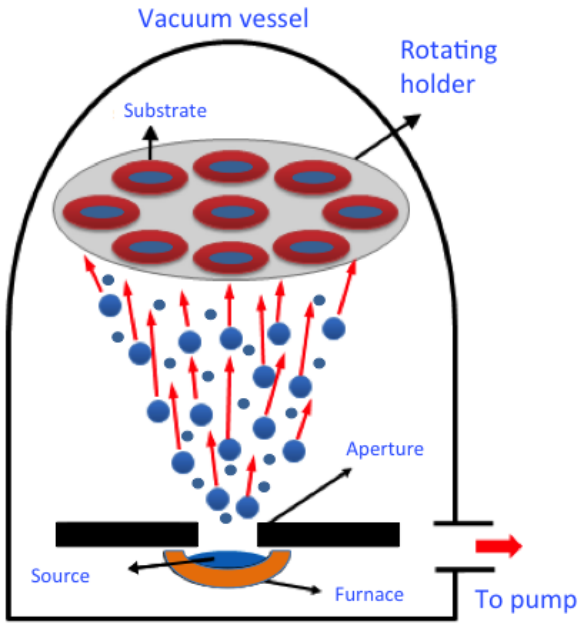

FIGURE 5.10
Schematics illustrating the thermal evaporation process

The substrate is mounted in or on a heater element, kept at the desired temperature to epitaxially grow films, and faced toward the heated source material. In the case of the fabrication of sulfides, the introduction of hydrogen sulfide at elevated pressures is essential for film formation. To avoid flooding of the chamber with oxygen or hydrogen sulfide, the main chamber is continuously pumped, as the reactive gas is introduced close to the substrate. Occasionally, a customized housing is used to confine the gas around the substrate. To obtain chips (semiconducting wafers,

solar cells or optical components) on the order of 10-20 nm, the height of the region with enhanced oxygen or hydrogen sulfide pressure must be comparable to its lateral extension*, i.e.*, the dimensions of the substrate. Otherwise, the metal vapors start scattering by increasing the thickness of this zone. Since the scattering cross section depends on the molecular weight, the composition becomes extremely pressure dependent [44]. If the gas pressure is further increased, the vapor does not penetrate this barrier and cannot reach the substrate to form the coatings, which are usually in the thickness range of angstroms to microns, and can be a single material or multiple materials in a layered structure. This method enables control not only of the thickness but also the uniformity, deposition rates, adhesion strength, real time rates, stress, grain structure and physical and chemical properties of OFMBBs.

Vapor-Liquid-Solid Mechanism

The growth of OFMBBs, either by CVD or thermal deposition, is typically described in terms of three main stages: (i) nucleation, (ii) crystal growth, and (ii) grain growth. The process whereby the molecules or atoms in the vapor phase come together to form a condensed entity is called nucleation [45]. In an emerging nucleus, the energetic contribution necessary to grow larger comes from the surface energy supplies (having a positive Gibbs free energy), until reaching a certain size, from which the surface effects become less dominant and the condensed phase continues to grow. The nucleation and growth of films on substrates is a complex phenomenon due mainly to the interactions between nucleation sites, adsorbed atoms (adatoms) and defects [45]. Three growth types characterize the film growth: (i) the Frank-van-der-Merwe growth type, where each layer is completed before the next layer is started; (ii) the Volmer-Weber growth type, where islands of the deposited material (several layers thick) form and eventually coalesce; and (iii) the Stranski-Krastanov growth type, which is a combination of the first two [45]. The first one establishes that complete layers grow sequentially but then islands begin to appear, whose growth is governed by the second growth type. In the first growth mechanism, the assumption is that the adsorbed atoms have a stronger attraction for the substrate than they do for one another, in contrast to that assumed by the second one. The mechanisms observed in a specific synthetic procedure can be rationalized in terms of the possible types of chemical bonding between the adsorbed molecules and the substrate.

In the case of the growth of one-dimensional crystals assisted by metal catalysts, the VLS mechanism that is the *sum* of these three growth types has been widely used for its simplicity and versatility when applied in many sulfides systems. The VLS mechanism posits that the metal catalyst deposited on the substrate forms droplets of liquid alloy at high temperatures by adsorbing vapor constituents. This is because the droplet surface possesses a relatively higher sticking coefficient, providing a preferred adsorption site for arriving vapor reactant [40]. When the temperature or vapor pressure starts fluctuating, the alloy is further supersaturated resulting in a solution with a component concentration higher than the equilibrium concentration. This subsequently leads to the precipitation of the component at the liquid–solid interface to attain the minimum free energy of the alloy system [46], giving rise to the one-dimensional crystal growth, which continues provided that the vapor components are supplied (see Figure 5.11). This process is similar to the Stranski-Krastanov growth type in the fact that the adsorbate films (beyond a critical layer thickness) continue growing through nucleation, and coalescence of adsorbate islands. In VLS, the vapor phase plays the role of carrying the solid components, the liquid phase of catalyst alloy, and the solid phase of precipitated one-dimensional structures. Given that the role of the droplet in the one-dimensional crystal growth is analogous to a catalyst in a chemical reaction, VLS growth is

also called catalysis growth.

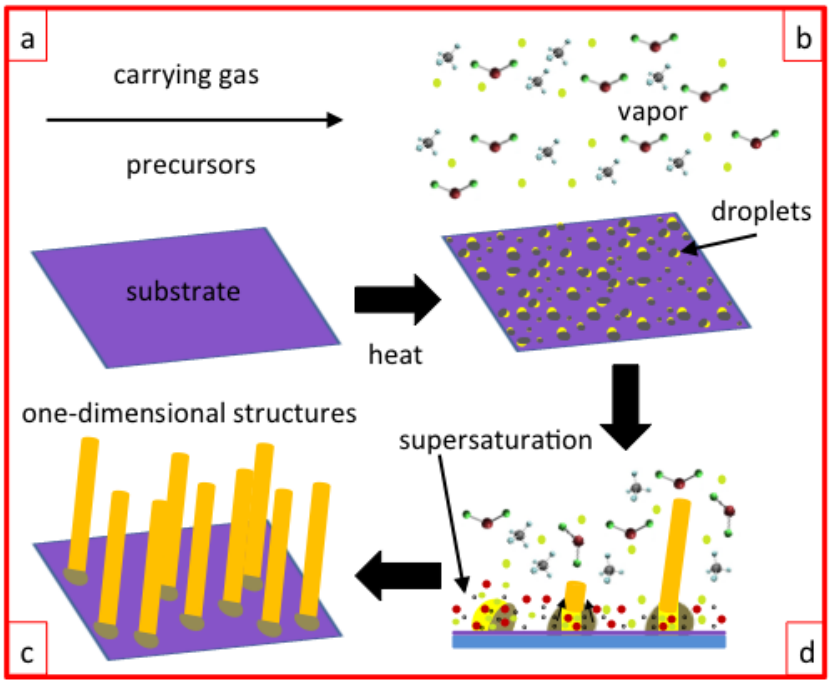

FIGURE 5.11
Schematics illustrating the growth of one-dimensional structures by VLS

It is noteworthy that the size and position of the catalyst can be related to the diameter and position of the structures, as the liquid phase is confined to the area of the precipitated solid phase [40]. Over the past few decades, this mechanism alone or in combination with vapor–solid–solid (VSS), liquid–solid–solid (LSS) or vapor-solid (VS) mechanisms, where the metal catalysts in solid form are exposed to vapor or liquid phase environments), has been employed to fabricate one-dimensional ZnO structures. For instance, Fan and co-workers [47] synthesized ordered arrays of spatially-separated ZnO pillars at large scale via a template-directed approach (using powdered ZnO, carbon monoxide and graphite), and described by VLS and VS. Using metal membranes as a lithography mask, the authors made the Au nanodisk arrays that are used as porous templates. They found that the pillars with 300 nm in diameter and 2 μm in height exhibit a long-term hexagonal order, and that the Au nanodisk array led its growth (see part a, b and c of Figure 5.12). The Au (usually staying at the growth fronts of the material) did not appear at the top ends of the pillars but at the base in the form of Au dots with diameters much smaller than those of ZnO pillars [47]. The authors proposed the following VLS-VS mechanism to explain their findings. At high temperatures (~800 °C, the substrate temperature), the Zn vapor produced by the reaction of ZnO powder with graphite and carbon monoxide is diffused toward the substrate site, where the original gold nanodisks are broken into smaller particles, which absorb the Zn atoms to form alloyed liquids. Supersaturation takes place enabling the precipitation and oxidation of Zn, thus a central ZnO nucleus is formed. Afterwards, newly arrived Zn atoms impinge and migrate on the surface of the pyramid. They will nucleate and integrate into a ZnO lattice at the peaks of the

pyramids that provide the lowest-energy sites. Zn atoms migrate to the base of the growing pillars or are desorbed. Then, ZnO tends to protrude from the center of the nuclei and grow into short pillars, which serve as preferential nucleation sites for further deposition of highly saturated Zn vapor and seeds for homoepitaxial growth of ZnO [47]. Finally, after continuous growth, well-defined pillar structures are obtained (see part d of Figure 5.12). VLS mechanism is a powerful tool to explain the mechanistic phenomena associated to the self-assembly of not only oxides, but also high-quality OFMBBs sulfides with controlled size, phase, composition and morphology.

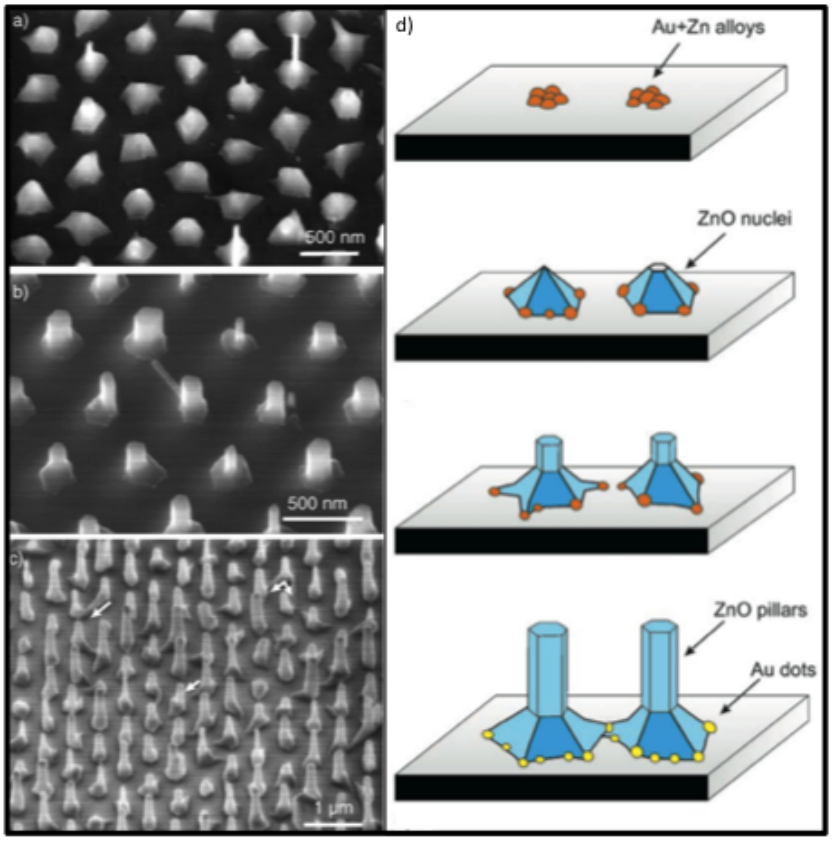

FIGURE 5.12
Schematics illustrating the growth of one-dimensional ZnO pillars by VLS and VS. Copyright © 2006. Reproduced with permission from Wiley-VCH Verlag GmbH & Co. KGaA

OFMBBs Sulfides

The nanofabrication of OFMBBs sulfides by CVD or thermal evaporation via the VLS mechanism offers the possibility of tuning their chemical, physical, magnetic, optical and electrical properties controlling, for instance, the anion deficiency and cation valence state [40]. The OFMBBs are also studied because their positive or negative ionically-charged terminated surfaces can induce spontaneous polarization across their thickness. In this regard, some novel morphologies that

exhibit dislocation-free surfaces with atomically-flat facets have been reported [10, 48]. Moreover, their diverse structure, new transport phenomena associated and striking characteristics render them more suitable for expanding the scope of applications in multiferroics, piezoelectricity, superconductivity, energy harvesting/conversion, optoelectronics, detectors, amperometric and optical bio-sensors, and energy storage. For instance, when OFMBBs with increased surface areas act as electrodes in LIBs technology and supercapacitors (SCs) [12,49], several advantages are achieved, including: (i) increase in electrode/electrolyte contact area per unit mass, enabling a higher lithium-ion flux across the interface and in turn higher charge/discharge rates for LIBs; and more ion adsorption sites for double-layer formation and charge-transfer reactions and in turn higher specific capacitance for SCs; (ii) shorter path lengths for ionic and electronic transport, resulting in a faster diffusion rate (*i.e.*, higher power); (iii) better accommodation of the mechanical strain and structural distortion generated from ion insertion/extraction and other reactions, which induces longer lifecycles; and (iv) the occurrence of new reactions that are not possible for materials with low surface areas [49]. The science behind the growth of one-dimensional manganese-based structures is of great interest to further develop new functional building blocks with large surface-to-volume ratios, and to promote their rationalized implementation in new-generation devices and smart bio-platforms.

Special interest has been devoted to fabricating anisotropic wurtzite-structured MnS NRs with non-conventional cross-sections due to their enhanced surface-to-volume ratio, which is larger than those reported in conventional NRs, and due to their high surface stability. Nanoribbons with one side flat and the other side saw-toothed are termed nanosaws (NSs). The striking morphology of these MnS structures can be used as customized nanocantilevers for probing scanning technology, and as ultraviolet-light sensors, field emitters, nanoresonators, photoconductive semiconductor switches, source light in LEDs, and anode materials in high-performance LIBs [50-53]. The synthesis of metastable single-crystal γ-MnS NSs films via the CVD process has been recently reported [10]. The films grew on (001)Si substrates, which were previously seeded with $AuCl_3$. The Au catalyst-covered Si substrates along with the precursors, $MnCl_2$ and sulfur powder, were placed into a fused silica tube in a hot-wall horizontal furnace. The amounts of sulfur and $MnCl_2$ were adjusted in order to obtain a 1:3 Mn:S molar ratio. $MnCl_2$ was positioned in the middle of the furnace (hot zone), where the temperature (~1273 K) was monitored; while the sulfur (downstream) and the Si substrate (upstream) were placed at certain distances from $MnCl_2$ (170 and 115–100 mm, respectively) and kept at ~673 K and 973–1123 K, respectively (see Figure 5.13 for a depiction of the apparatus and temperature profile of the hot-wall horizontal furnace employed). The reaction tube was evacuated down to 465 mPa to purge oxygen, heated to 1273 K, and filled to 46.5 Pa with a constant Ar flow at 20 sccm, which was used as carrying gas to transport the sublimated vapor to the cooler regions within the chamber for deposition. After 1 h, the $MnCl_2$ and S are fully consumed. The tube was then left to cool spontaneously to RT. Following this procedure, electron microscopy shows that the thickness of films were ~25 mm (see Figure 5.14). These films present a densely populated surface with spaghetti-like NRs, with the catalytic material on the ends thereof (see Figure 5.15), indicating that they grew following a catalyst-based mechanism. γ-MnS NRs possess a high aspect ratio (AR) with widths falling in the range of 100–350 nm and lengths over 25 mm. SEM images also reveal that the majority of the NRs observed are comb-shaped, *i.e.*, NRs with one side flat and the other side saw-toothed. Similar morphologies were also obtained by Ma et al. working with wurtzite metal chalcogenides via CVD process [51,54]. *γ*-MnS NBs are also present in the as-grown samples, but they are not the dominant component. Both saw- and belt-like nanostructures grown at the same temperature range possess a common nucleation site, indicating that they are nucleated and grown as bunches randomly dispersed on the substrate [54].

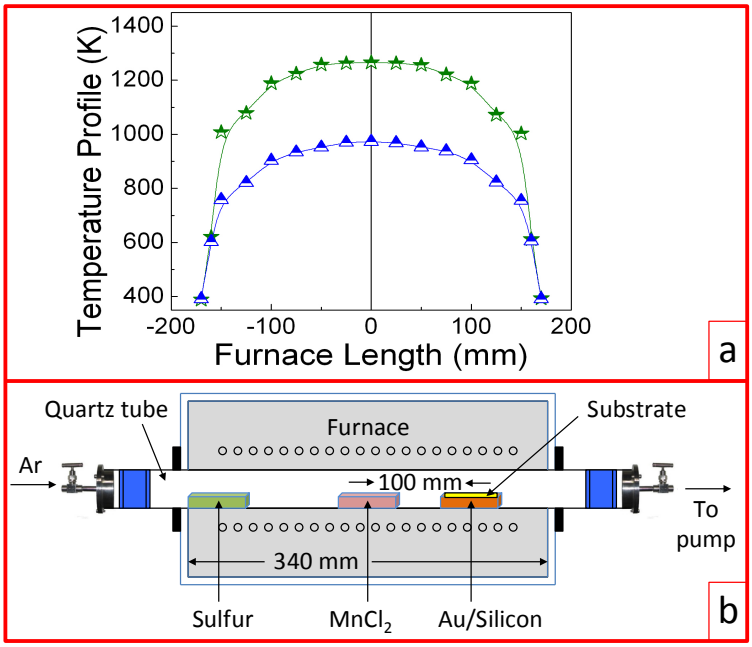

FIGURE 5.13
Temperature profile (a) and a depiction of apparatus (b) of the hot-wall horizontal furnace for the fabrication of films of single-crystal γ-MnS NSs on silicon substrates

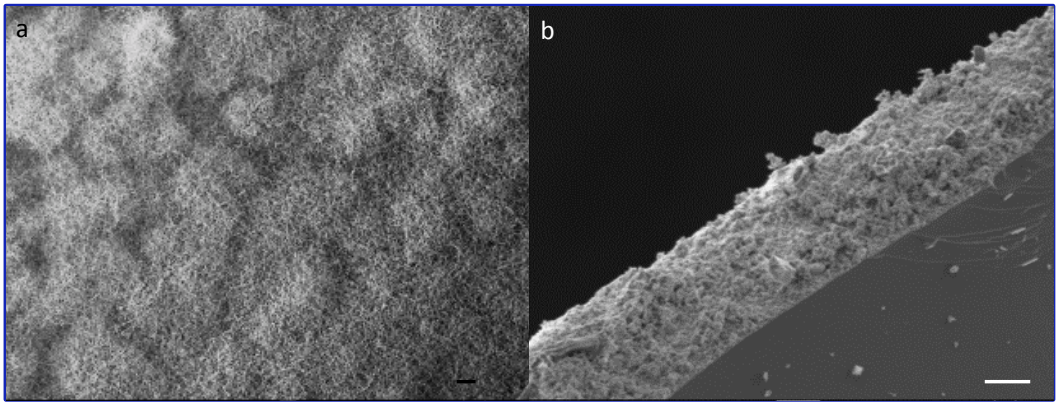

FIGURE 5.14
Field-emission SEM images γ-MnS films on silicon substrates. The scale bar in (a) is 100 µm and in (b) is 10 µm

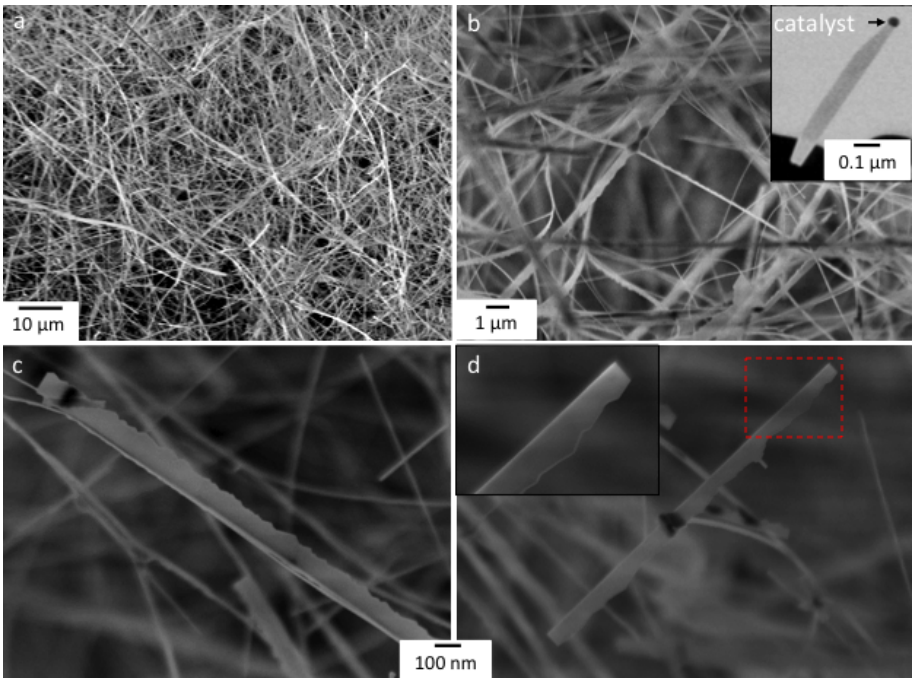

FIGURE 5.15
Field-emission SEM images of γ-MnS NSs. Insets in (b) and (d) show the catalytic and a close-up of an individual NS, respectively. Adapted from Ref. [10]. Copyright © 2014. Reproduced with permission from Royal Society of Chemistry

As described in the previous section, the morphology of these nanostructures can be changed by varying the experimental parameters. Thus, reducing the concentration of oxygen traces, controlling the evaporation rate of precursors and achieving more uniform layers of catalytic material on substrate, wires at microscale and saws at nanoscale were obtained in certain regions of the films. Nanobelts resembling square lollipops were produced by increasing the partial vapor pressures (see Figure 5.16) within the reacting tube. Similar exotic morphologies of metal sulfides were also observed by Prof. Wang's research group. Here, the NWs, NBs and NSs grow from a single nucleation site and are governed by the VLS and VS mechanisms.

The authors used high-resolution transmission electron microscopy (HRTEM) to determine the geometry of the nanostructures. They found that the geometrical shape of the γ-MnS nanostructures is belt-like with uniform widths (in the range of 80 to 250 nm) along their length. The presence of catalytic material on the ends of the NBs indicates that VLS process is the prevailing growth mechanism (see Figure 5.17). The ripple-like contrast observed in the HRTEM images is a result of the strain generated from the bending of the belt, since the degree of flexibility of the NBs is associated to their thickness. The authors also related this fact to the formation of stacking faults and twining occurring as a mechanism to stabilize the growth of the nanostructures, which is typical in thermal evaporation. Statistical analyses on different regions of the films show that the dominant morphology in the products is saw-like, which resembles parallel triangles (~10–50 nm high) grown along the NSs axes, similar to perfectly aligned nanocantilever arrays used in probing scanning technology [10].

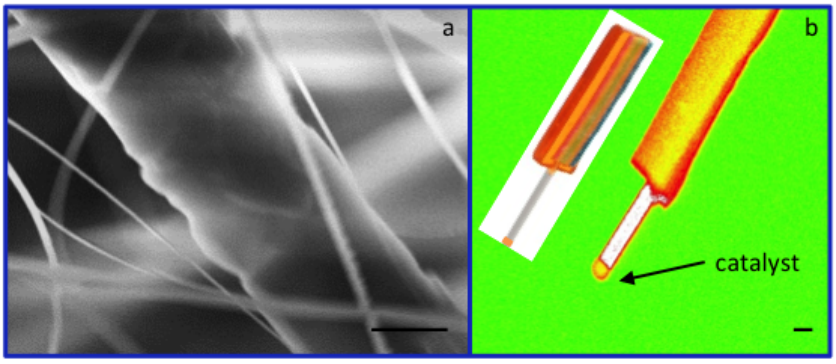

FIGURE 5.16
Field-emission SEM images of γ-MnS with different morphologies. Inset in (b) is a square lollipop that resembles the MnS nanostructure synthesized by CVD. The scale bar in (a) is 1 µm and in (b) is 100 nm

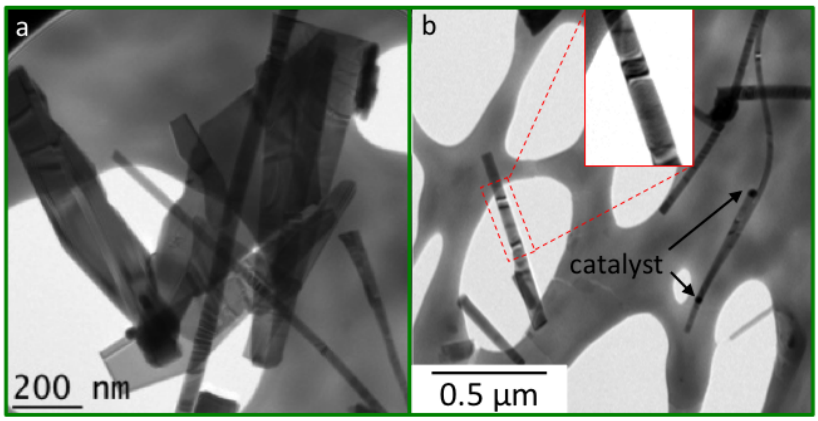

FIGURE 5.17
High-resolution TEM images of γ-MnS nanostructures. Inset in (a) is a closer view of an individual nanobelt

The ends (tips) of the cantilevers are atomically rough (see the black arrowhead in the middle inset of Figure 5.18). The surfaces of the NSs are clean, smooth, and atomically resolved (see left upper inset of Figure 5.18). Hence, this method provides an efficient route to develop 1D building blocks without any sheathed amorphous phase, having low degree of interdiffusion between the material itself and the surrounding medium. An inner view into the nanostructures (see lower and left upper insets of Figure 5.18) accompanied with the SAED analyses indicates three important factors. Firstly, the NSs grow along the [0110] direction with top and bottom surfaces ±(2110) and side surfaces (0001). Secondly, the growth direction of the NSs teeth is along [0001] with an interplanar spacing of 0.32 nm. Finally, the NSs are single crystal with wurtzite structure.

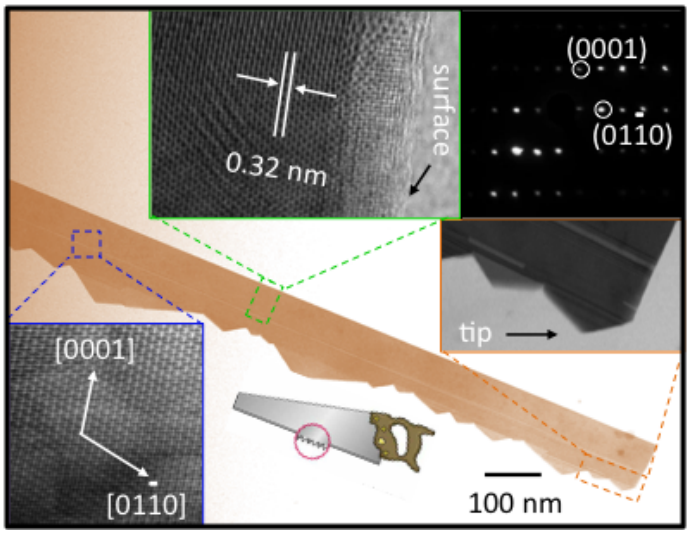

FIGURE 5.18
High-resolution TEM image of a representative γ-MnS NS. The left upper, middle, and right lower insets show the surface, the tip and interior, respectively, of an individual γ-MnS NS. The right upper inset shows the SAED pattern. The left lower is a saw whose blade resembles the MnS NSs synthesized by CVD. Adapted from Ref. [10]. Copyright © 2014. Reproduced with permission from Royal Society of Chemistry

In order to gain more insight on the uniformity of the cross- sectional thickness, width of tip, and dislocations or defects present in γ-MnS NSs, the authors carefully examined several NSs by illuminating them with 200 kV electrons for a somewhat longer time, but not enough to cause any increase of planar induced defects, damage, phase transformation or amorphous carbon deposition during the exposure [10]. They found that the NSs are transparent to the TEM grid, suggesting that they are a few tens of nanometers thick (see Figure 5.19). In fact, the backsaw thickness resulted to be in the range of 30 to 50 nm, and width-to-thickness ratios of ~3.3 to 7.0. The thickness was significantly reduced from the end of backsaw to the teeth (radially), reaching values as low as few nanometers. In this region, the NS (surface encompassed by the teeth) is structurally uniform and highly crystalline with two growth directions: [0110] and [0001]. In addition, no dislocations were found, but rather single atomic-thick stacking faults along the NS and teeth axes. A closer view into the tip of teeth shows that its surface is seamless having a wurtzite structure (according to the fast Fourier transform (FFT) indexation), and its width is approximately a couple of atoms thick. A unit-cell model for the hexagonal phase of MnS is shown in the inset of Figure 5.19. The projected position of the Mn atoms in the unit cell correlates well with the TEM projection image taken on the end of tip and oriented along (2110). The authors attributed the asymmetric growth of the NRS to the polarization of the *c*-plane [10], which is explained as follows below. It is known that the chalcogen polar surfaces in chalcogenides (wurtzite ZnS and CdSe) are unreactive [50, 51, 55], and the (0001)-Zn and -Cd-terminated surfaces are chemically reactive, *i.e.*, they adsorb methanol, formaldehyde and formic acid, and ZnS and CdSe vapors [10]. These active surfaces are responsible for growing saw-like structures (such as one- and double-sized NSs), acting as the self-catalyst. Thus, polar surfaces induce the formation of asymmetric NRs. The authors assumed that the saw-like nature of wurtzite-structured MnS, consisting of alternating layers of oppositely charged ions

((0001)-Mn^{2+} and (0001)-S^{2-}) and stacked parallel to the c-axis, is induced by both the surface polarization and surface termination (see inset of Figure 5.19).

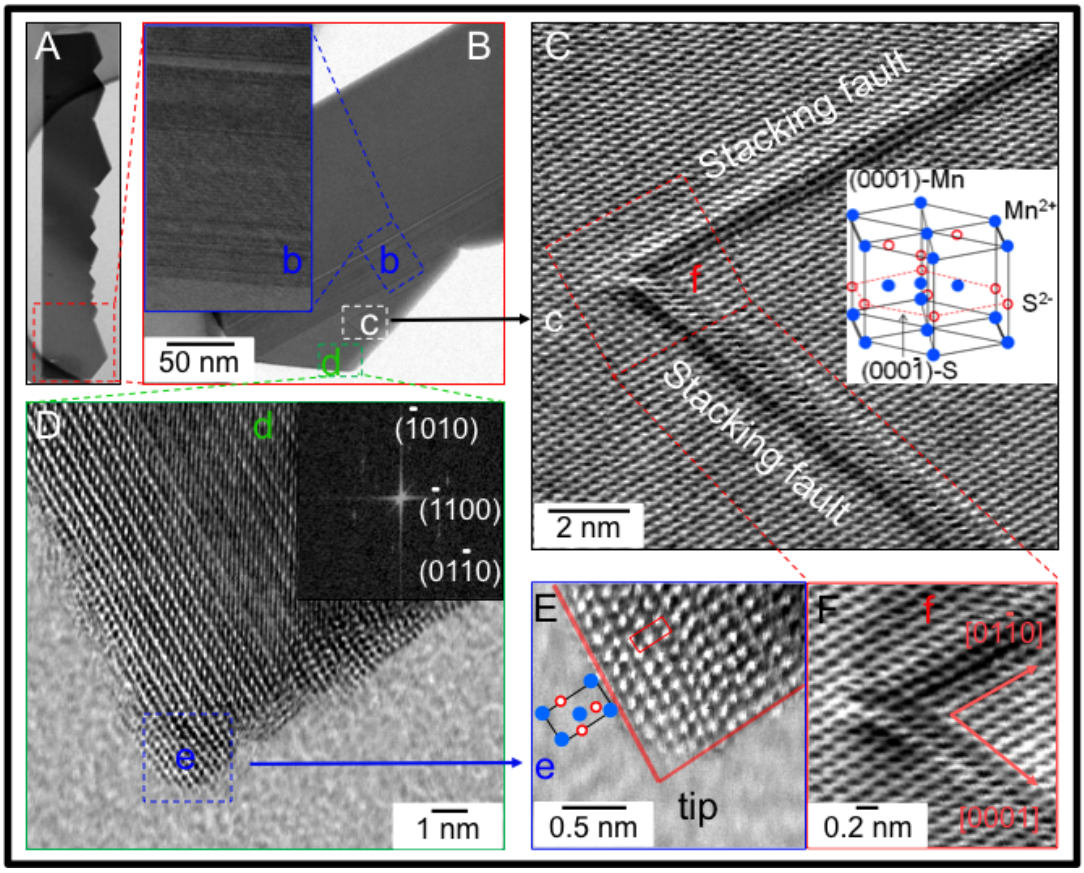

FIGURE 5.19
HRTEM image of a representative γ-MnS NS (A). A closer view of (A) that shows the interface between the backsaw and teeth is displayed in (B) and the inset therein. Closer views of (B) that show two stacking faults along the NS and teeth axes are displayed in (C) and (F). A unit-cell model of γ-MnS is shown in the inset of (C). Lattice-resolved images of (B) that shows the width of the nanotips are displayed in (D) and (E). The FFT image corresponding to (D) is shown in the inset of (D). Inset in (E) shows the projected position of the Mn atoms of the unit-cell model of γ-MnS shown in the inset of (C). Copyright © 2014. Reproduced with permission from Royal Society of Chemistry

Even though the ionic crystal composed of tetrahedrally-coordinated Mn^{2+} and S^{2-} layers exhibits an accumulating normal dipole moment (as a result of the surface polarization), the γ-MnS NSs are stable without facets or massive surface reconstructions.

Anisotropic OFMBBs sulfides can be grown via CVD following two stages. First, the NRs are rapidly formed along [0110] with top and bottom surfaces ±(2110), and side surfaces (0001), following a bottom-up Au-catalyst-based approach governed by the VLS growth mechanism. Second, the subsequent growth (self-catalyzed from the Mn-terminated surface) of the teeth is oriented along [0001], which is a consequence of the surface polarization and surface termination of the wurtzite

structure. Although these one-dimensional nanostructured sulfides are structurally stable, they are sensitive to environmental changes, surface chemistry and photo-oxidation. In order to circumvent this hurdle, Beltran-Huarac and co-authors encapsulated the reactive MnS with sp^2-bonded carbon to generate a physical barrier and endow the core with an enhanced stability and a more efficient surface passivation [6]. The authors used the same experimental setup and added a continuous methane flow of ~5 sccm. The SEM images of this core/shell system are depicted in Figure 5.20. The γ-MnS/C films are a few micrometers thick and densely populated with spaghetti-like NWs. These γ-MnS/C NWs possess a high aspect ratio with diameters falling in the range of 60-100 nm and lengths over 100 µm [6]. However, they break into smaller rods when manipulated (transferred onto TEM grids), thus reducing their aspect ratio [2]. This indicates that they are brittle. No sign of the catalytic material is found on the top end of individual γ-MnS/C NWs, suggesting that they grew with the catalyst at the base (*i.e.*, base- growth model). Figure 5.20 shows that γ-MnS/C NWs consist of a core/shell structure with hexagonal cross-section, or hexagonal NWs uniformly covered by a smooth shell layer.

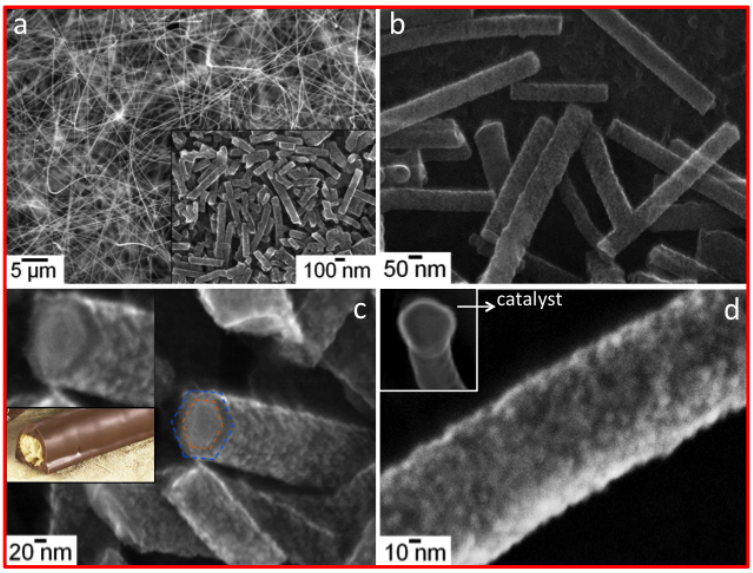

FIGURE 5.20
Field-emission-SEM images (a-d) of γ-MnS/C NWs. Inset in (a) shows how the NWs look like after they were transferred to a TEM grid. Upper inset in (c) shows a close-up of an individual NW. Lower inset in (c) is a rod-like bar of chocolate that resembles the γ-MnS/C NWs synthesized by CVD. Inset in (d) shows the catalyst at the end of an individual NW. Adapted from Ref. [6]. Copyright © 2014. Reproduced with permission from American Chemical Society

These features were highlighted by overlaying two concentric hexagons on the image of Figure 5.20c. An orange hexagon was assigned to the core material and a larger blue hexagon for the shell material. The authors suggested that the perfectly radial cuts observed in the NWs originated from the shear stress produced by the transfer of the NWs from mother substrates to TEM grids [6].
The conformal coating of the shell material (light contrast) onto the core material (dark contrast) was further confirmed by transmission electron microscopy (see Figure 5.21). The outer diameter of the NWs is around 60− 100 nm, whereas the inner diameters are between 20 and 50 nm. The

width of the interface between the shell and core is <0.5 nm, indicating that it is not only thin, but also smooth and abrupt [6]. This method provides an efficient route to develop core/shell OFMBBs systems with low degree of interdiffusion between the core and shell material, even after harsh annealing treatments. Figure 5.21 also enables us to discriminate the lattice fringes of the constituent phases, with *d*-spacings of ~ 0.3347 and 0.2991 nm characteristic of graphitic carbon and wurtzite MnS, respectively [56].

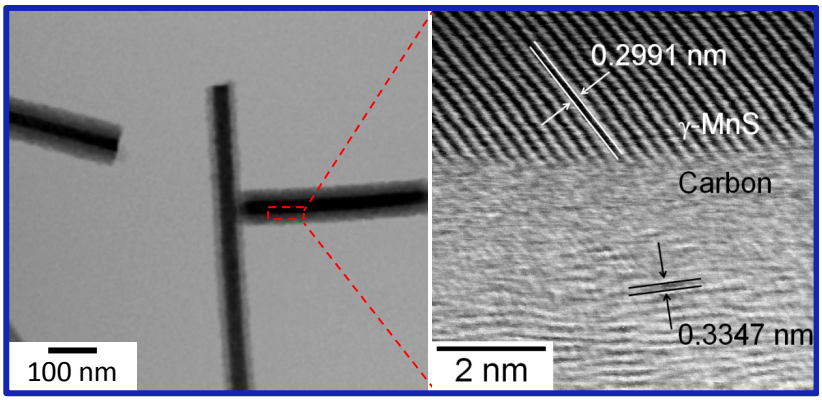

FIGURE 5.21
High-resolution TEM image (left) of a representative γ-MnS/C NW and its corresponding closer view (right) showing the interface between the γ-MnS and carbon shell. Adapted from Ref. [6]. Copyright © 2014. Reproduced with permission from American Chemical Society

These results indicate that the growth of core/shell γ-MnS/C NWs is governed by VLS, similar to the growth of γ-MnS NSs. The authors explained the core/shell system formation with the arguments that follow. At the growth temperature (~1123 K), elemental Au and Ni nanoparticulate forms bimetallic Au−Ni alloy droplets (AADs), which exhibit a synergistic effect of high catalytic activity for sulfides and hydrocarbons. At the liquid−solid interface of supersaturated AADs, the MnS synthesis reaction takes place, as follows:

$$MnCl_2 + 3S \rightarrow MnS + S_2Cl_2 \quad (1)$$

Similarly, hydrogen abstraction reactions of CH_x species take place at the AADs, leading to the formation of graphitic carbon. The net effect is the formation of amorphous Mn−S−C NWs with the AADs at base. Upon subsequent annealing, the amorphous Mn−S−C NWs undergo crystallization of the γ-MnS accompanied by the precipitation of graphitic C to the surface, giving rise to the γ-MnS/C NWs, as shown in Figure 5.22.
These sulfides have been recently proposed as novel phosphors in LED technology due to their ability to emit visible light efficiently, and their effective downconversion process [14]. The optical tunability of one-dimensional MnS is of great importance in this respect. Kim and co-workers [57] doped MnS NWs with Cd ions (5-10 % doping level) via CVD process. They used $MnCl_2$ and CdS powders as precursors, which were placed within the reactor of a tube furnace under ambient pressure and controlled temperature (900-1200 K).

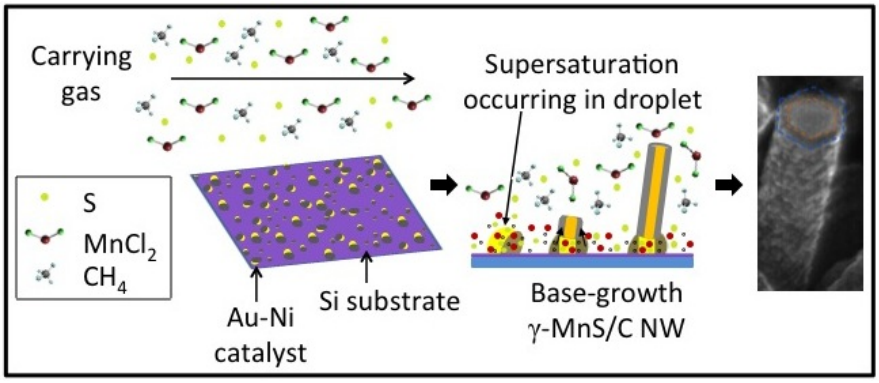

FIGURE 5.22
Depiction illustrating the VLS growth mechanism for the synthesis of core/shell γ-MnS/C NWs. Adapted from Ref. [6]. Copyright © 2014. Reproduced with permission from American Chemical Society

The NWs are 80 nm in diameter exhibiting straight wire morphology and smooth surfaces (see Figure 5.23). The EDS analysis shows that both 5 and 10 % Cd are homogeneously distributed along the cross section of the NWs [57]. The diameter of the NWs falls in the range of 40-60 nm, with an average value of 50 nm. Negligible defects are observed in the lattice planes despite their rough surface (see Figure 5.23e). The single-crystal NWs grew along the [110] direction and governed by the VLS mechanism. The authors evaluated the incorporation of Cd ions into the host MnS via PL in the temperature range of 7-300 K, using excitation photon energy of 3.815 eV. The PL spectra depicted in Figure 5.24 shows that the broad emission band observed at 2.9 eV is similar to the band gap of the bulk [58], and can be ascribed to the band-edge emission band that involves the excited states (including $^4T_1$, $^4T_2$ and $^4A_1$) of the Mn^{2+} ions [59]. The other emission band observed at around 1.6 eV originates from the decay of the impurity-perturbed excited states of the Mn^{2+} ions, generated by the usual *d-d* energy transfer from the higher excited states [60], and is completely absent at temperatures above ~150 K. As the Cd-ion content increases, the band-edge emission becomes broader, and the relative intensity of the band at 1.6 eV tends to decrease (when compared to the band-edge emission band) [57]. A new emission band at 2.13 eV is observed in the NWs with 10% Cd doping (see Figure 5.24b), which is attributed to the *d-d* ($^4T_1 \rightarrow {}^6A_1$) transition of the Mn^{2+} ions at the tetrahedral sites [61]. The average decay times of the Mn^{2+} emission band at 1.6 eV (7 K and 266-nm excitation) for the un-doped and 10% Cd-doped MnS NWs are 40 and 30 μs, respectively, signifying a decrease with increasing Cd content. These values remain nearly the same until 100 K.

Mochizuki and Takayama [20] suggested that the 1.6 eV emission band originating from the decay of the Mn^{2+} excitons is related to the impurity-perturbed states of the Mn^{2+} ions, and that its appearance at low temperatures (below 150 K) is correlated with the antiferromagnetic spin-ordering (T_N~150 K for the bulk). Note that the energy transfer rate between the neighboring Mn^{2+} ions is smaller in the spin-ordered than in the paramagnetic phase. Geode and co-workers [62] found that the T_N of the Cd-doped MnS bulk decreases with increasing Cd content, *i.e.*, 152 K for MnS, 127 K for 10% Cd-doped MnS, and 105 K for 20% Cd. They also reported the effective decay times of ~140 μs for MnS and ~60 μs for 20% Cd. Thus, the energy transfer between neighboring Mn^{2+} ions in OFMBBs sulfides is substantially influenced by the antiferromagnetic spin-ordering [57].

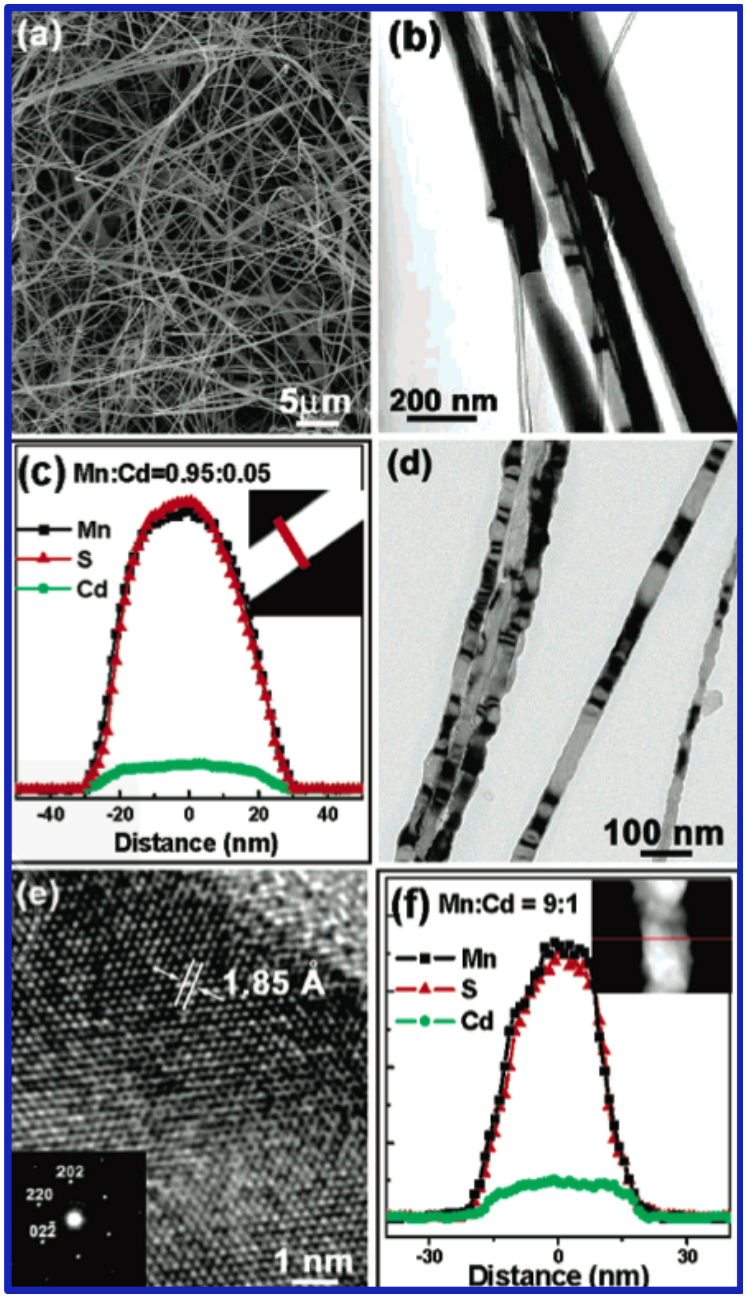

FIGURE 5.23
SEM image (a) of 5% Cd-doped MnS NW films. TEM image (b) showing the smooth surface and an average diameter of 80 nm. Line-scanned EDS profile (c) of an individual NW showing 5% Cd composition. TEM image (d) of 10% Cd-doped MnS NWs showing the rough surface and an average diameter of 50 nm. Atomically resolved image (e) reveals the highly crystalline lattice planes of MnS NWs. The inset corresponds to the SAED pattern, showing the [110] growth direction. Line-scanned EDS profile (f) of an individual NW showing 10% Cd composition.

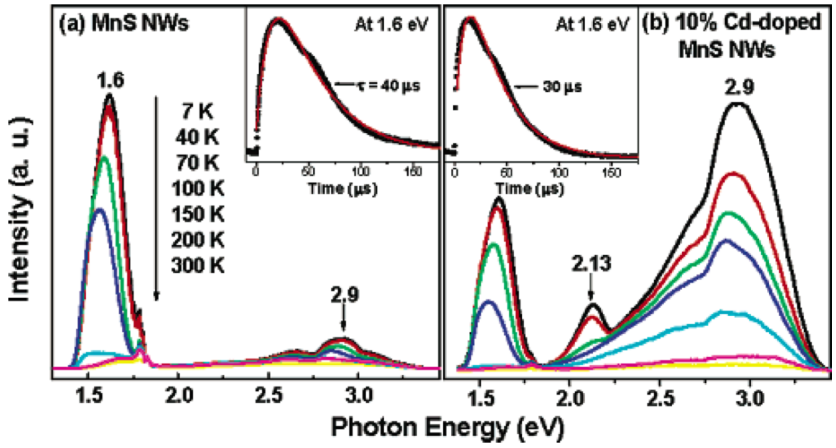

FIGURE 5.24
Temperature-dependent PL spectra of MnS (a) and 10% Cd-doped MnS (b) NWs. The insets correspond to the time-resolved spectra of the emission band at 1.6 eV. Copyright © 2006. Reproduced with permission from American Chemical Society

More recently, it has been reported that the optical properties of OFMBBs sulfides can be tuned by changing their morphology. This enables a controlled release of the strain of NWs from their crystalline structure, resulting in a shift of the maximum PL intensity to higher energies [63]. In this regard, the PL response of γ-MnS nanosaws having a wurtzite structure was evaluated on a macroscopic scale [10]. The PL spectra recorded in the temperature range of 10-300 K are depicted in Figure 5.25. The PL spectra at 300 K show one predominant yellowish-orange emission band peaking at ~2.15 eV at, which is associated to the radiative recombination of electrons in shallow traps of surface localized states, and photogenerated holes caused by stacking faults present in the NSs (see Figure 5.19c). The nanostructures also show a relatively weak near band edge emission band centered at ~3.34 eV, and a defect-related emission band at ~2.88 eV, analogous to that reported by MnS NWs [57]. The near band edge emission of NSs is blue-shifted ~16 nm when compared to the bulk value (~3.20 eV) [24]. This shift is correlated to the morphology of the nanosaws, specifically to the tiny width, approximately a couple of atoms thick, of the γ-MnS NSs tips, which gives rise to a quantum confinement effect. This finding is compatible with those reported by Ma et al. working with CdSe NSs [51]. Another factor that may contribute to this blue shift is related to the small thickness of the NSs backsaws. The authors attributed the origin of the defect-related emission at ~2.88 eV to the higher-level transition of γ-MnS from the surface defects [18, 64]. The fact that the PL intensity of the surface defect-induced emission at ~2.13 eV is four orders of magnitude stronger than the exciton-related emission band at ~3.34 eV, indicates the presence of a high density of single stacking faults on the NSs surfaces.
The redshift (~4 nm) of the band at 2.15 eV at temperatures below 60 K is associated to its shallow-trap emission character. Figure 5.25 shows that the yellowish-orange emission band experiences a remarkable drop in PL intensity as the temperature decreases. A relatively small change in PL intensity is observed over the temperature range from 300 to 180 K. A significant increase in PL intensity is observed at lower temperatures. The integrated PL intensity is doubled from 100 to 10 K, which corresponds to the transfer of electrons trapped in the donor states and that are promoted towards the conduction band [10]. The authors assumed that the interaction between neighboring Mn^{2+} ions contributes to the carrier transfer, which is influenced by the

antiferromagnetic spin-ordering (similar to MnS nanowires) given that more prominent PL intensity changes were observed below 100 K (T_N = 90 K) [57, 65]. Through a thermally activated carrier-transfer model [66], the authors determined that the position of the donor level with respect to the conduction band is ~40 meV, which correlates well with the increased surface-to-volume ratio in γ-MnS NSs. This signifies that the donor state is associated to the surface states of the NSs, and that the carrier transfer corresponds to a donor–acceptor pair transition [67]. The authors also evaluated the PL kinetics of the emission band at 2.13 eV and found a decay time of ~44 ms, almost three times shorter than that reported for bulk MnS. This indicates that the enhanced surface area of γ-MnS NSs is responsible for the acceleration of the non-radiative energy relaxation rate due to the energy transfer from the excited Mn-states to surface states [10].

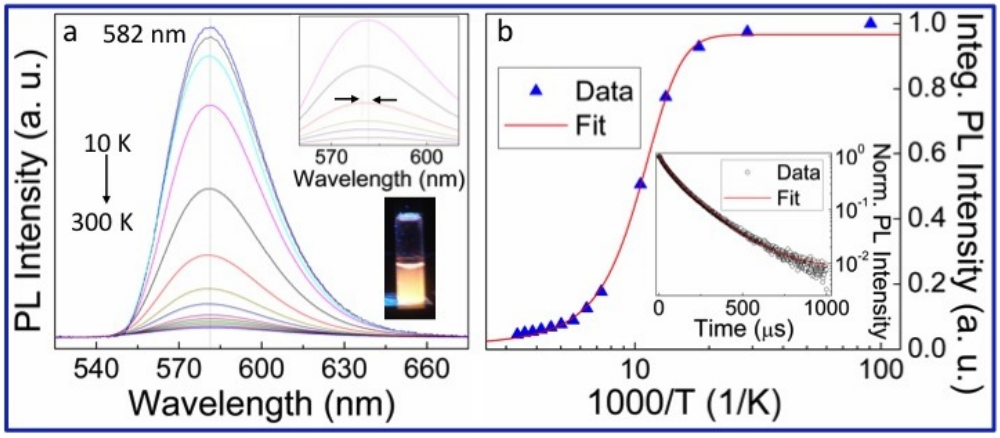

FIGURE 5.25
Temperature-dependent PL spectra (a) of γ-MnS NSa excited with a 3.81 eV He–Cd pulsed laser. The redshift of the yellowish-orange emission band is shown in the upper inset. The lower inset shows the optical image of γ -MnS NSs dispersed in aqueous solution as viewed under UV light at 300 K. Emission band intensity evolution as a function of temperature (b) fitted to Equation (2). Inset in (b) shows the PL decay curve fitted with a bi-exponential function. Copyright © 2014. Reproduced with permission from Royal Society of Chemistry

Accordingly, micro- and large-scale observations indicate that the unique optical properties of OFMBBs sulfides deposited by CVD are related to their striking geometry (in wire, belt and saw forms) and impurity doping, and most importantly remain structurally stable even at low temperatures. Unlike carbon nanotubes, whose metallic and semiconducting characteristics depend on the helical angle of the graphitic wall, the OFMBBs sulfides are semiconducting and present a well-defined band structure with high PL quantum yields.

Conclusion

In summary, the anisotropic nature and phenomena induced by surface polarization of OFMBBs sulfides allow tuning of their structural and optical properties. Single-crystal MnS nanofibers substantially reduce the grain boundary scattering present in polycrystalline MnS, which affects its PL response (and in turn its performance when used as a functional light source in optoelectronic

devices) due to the high density of nanosized grains distributed across the surface. The crystal structure, diameter, length, composition, impurity or doping level, defect concentration, nature of facets, size and growth direction of OFMBBs sulfides (in wire, belt or saw forms) influence their ability to absorb and emit light as well as their correlated downconversion. Encompassing the bottom-up approaches available in literature, VLS was found to be the most suitable for obtaining highly-crystalline and dislocation-free structural surfaces in sulfides, which also exhibit atomically-flat facets and tailorable structural characteristics. Sulfides induce spontaneous polarization due to their enhanced positive or negative ionically-charged terminated surfaces. This effect is accounted for in terms of the principle of minimum total energy in the OFMBB surfaces and their corresponding divergence (resulting from spontaneous polarization and elasticity). The self-catalyzed process is an alternative mechanism for the growth of OFMBBs in the absence of foreign metallic catalysts. It is noteworthy that these wurtzite nanostructures are as structurally stable as their bulk counterparts grown by CVD. This review represents a comprehensive synopsis that leads to a better understanding of the unusual *d*-*d* energy transfer phenomena caused by the excited states of high-spin Mn ions, which are critical in the performance of magneto-optic, spintronic and nanoelectronic devices.

Acknowledgements

This work was supported in part by PR NASA EPSCoR (NASA Cooperative Agreement NNX13AB22A and NNX15AK43A) and the Institute for Functional Nanomaterials (NSF Grant 1002410).

References

1. Xia Y, Yang P, Sun Y, Wu Y, Mayers B, Gates B, et al. One-dimensional nanostructures: Synthesis, characterization, and applications. Advanced Materials 2007; 15(5) 353-389.
2. Deng Z, Tong L, Flores M, Lin S, Cheng J, Yan H, et al. High-quality manganese-doped zinc sulfide quantum rods with tunable dual-color and multiphoton emissions. Journal of American Chemical Society 2011; 133(14) 5389-5396.
3. Duan X, Huang Y, Cui Y, Wang J, Lieber CM. Indium phosphide nanowires as building blocks for nanoscale electronic and optoelectronic devices. Nature 2001; 409(6816) 66-69.
4. Pan ZW, Dai ZR, Wang ZL. Nanobelts of Semiconducting Oxides. Science 2001; 291(5510) 1947-1949.
5. Chopra NG, Luyken RJ, Cherrey K, Crespi VH, Cohen ML, Louie SG, et al. Boron Nitride Nanotubes. Science 1995; 269(5226) 966-967.
6. Beltran-Huarac J, Resto O, Carpena-nuñez J, Jadwisienzak WM, Fonseca LF, Weiner BR, et al. Single-Crystal γ-MnS Nanowires Conformally Coated with Carbon. ACS Applied Materials & Interfaces 2014; 6(2) 1180-1186.
7. Ge J, Wang J, Zhang H, Li Y. A General Atmospheric Pressure Chemical Vapor Deposition Synthesis and Crystallographic Study of Transition-Metal Sulfide One-Dimensional Nanostructures. Chemistry A European Journal. 2004; 10(14) 3525-3530.
8. Zhang F, Wong SS. Controlled Synthesis of Semiconducting Metal Sulfide Nanowires. Chemistry of Materials 2009; 21(19) 4541-4554.

9. Beltran-Huarac J, Carpena-Nuñez J, Barrionuevo D, Mendoza F, Katiyar RS, Fonseca LF, et al. Synthesis and transport properties of $La_{0.67}Sr_{0.33}MnO_3$ conformally-coated on carbon nanotubes. Carbon 2013; 65 252-260.
10. Beltran-Huarac J, Palomino J, Resto O, Wang J, Jadwisienczak WM, Weiner WR, et al. Highly-crystalline γ-MnS nanosaws. RSC Advances 2014; 4 38103-38110.
11. a) Iijima S. Helical microtubules of graphitic carbon. Nature 1991; 354 56-58.
    b) Li X, Wang X, Xiong Q, Eklund PC. Mechanical properties of ZnS nanobelts. Nano Letters 2005; 5(10) 1982-1986.
    c) Fang X, Bando Y, Shen G, Ye C, Gautam UK, Costa PMFJ, et al. Ultrafine ZnS nanobelts as field emitters. Advanced Materials 2007; 19 2593-2596.
12. a) Zhen Z, Xie J. Development of Manganese-Based Nanoparticles as Contrast Probes for Magnetic Resonance Imaging. Theranostics 2012; 2(1) 45-54.
    b) Adams DM, Brus L, Chidsey CED, Creager S, Creutz C, Kagan CR, et al. Charge transfer on the nanoscale: current status. The Journal of Physical Chemistry B 2003; 107(28) 6668-6697.
    c) Sarkar I, Sanyal MK, Kar S, Biswas S, Banerjee S, Chaudhuri S, et al. Ferromagnetism in zinc sulfide nanocrystals: Dependence on manganese concentration. Physical Review B 2007; 75 224409.
    d) Zhang N, Yi R, Wang Z, Shi R, Wang H, Qiu G, et al. Hydrothermal synthesis and electrochemical properties of alpha-manganese sulfide submicrocrystals as an attractive electrode material for lithium-ion batteries. Materials Chemistry and Physics 2008; 111 13-16.
13. Yin J, Gao F, Wu Y, Wang J, Lu Q. Synthesis of Mn_3O_4 octahedrons and other manganese-based nanostructures through a simple and green route. CrystEngComm 2010; 12 3401-3403.
14. Kennedy SW, Harris K, Summerville E. Mechanisms of thermal transformation of zinc blende to [NaCl] in MnS crystals. Journal of Solid State Chemistry 1980; 31(3) 355-359.
15. Yang X, Wang Y, Wang K, Sui Y, Zhang M, Li B, et al. Polymorphism and Formation Mechanism of Nanobipods in Manganese Sulfide Nanocrystals Induced by Temperature or Pressure. Journal of Physical Chemistry C 2012; 116(5) 3292-3297.
16. Biswas S, Kar S, Chaudhuri S. Effect of the precursors and solvents on the size, shape and crystal structure of manganese sulfide crystals in solvothermal synthesis. Materials Science and Engineering: B 2007; 142(2-3) 69-77.
17. Zhang P, Zeng Q, He X, Tang H, Huang K. Preparation of γ-MnS hollow spheres consisting of cones by a hydrothermal method. Journal of Crystal Growth 2008; 310(18) 4268-4272.
18. Ren Y, Gao L, Sun J, Liu Y, Xie X. Facile synthesis of gamma-MnS hierarchical nanostructures with high photoluminescence. Ceramics International 2012; 38(1) 875-881.
19. Yang X, Wang Y, Sui Y, Huang X, Cui T, Wang C, et al. Size-Controlled Synthesis of Bifunctional Magnetic and Ultraviolet Optical Rock-Salt MnS Nanocube Superlattices. Langmuir 2012; 28(51) 17811-17816.
20. Lei S, Tang K, Yang Q, Zheng H. Solvothermal Synthesis of Metastable γ-MnS Hollow

Spheres and Control of Their Phase. European Journal of Inorganic Chemistry 2005; 2005(20) 4124-4128.

21. Ma W, Chen G, Zhang D, Zhu J, Qiu G, Liu X. Shape-controlled synthesis and properties of dandelion-like manganese sulfide hollow spheres. Materials Research Bulletin 2012; 47(9) 2182-2187.
22. Wang S, Li K, Zhai R, Wang H, Hou Y, Yan H. Synthesis of metastable γ-manganese sulfide crystallites by microwave irradiation. Materials Chemistry and Physics 2005; 91(2-3) 298-300.
23. Lu J, Qi P, Peng Y, Meng Z, Yang Z, Yu W, et al. Metastable MnS Crystallites through Solvothermal Synthesis. Chemistry of Materials 2009; 13(6), 2169-2172.
24. Jun Y, Jung Y, Cheon J. Architectural Control of Magnetic Semiconductor Nanocrystals. Journal of American Chemical Society 2002; 124(4) 615-619.
25. Zhang C, Tao F, Liu GQ, Yao LZ, Cai WL. Hydrothermal synthesis of oriented MnS nanorods on anodized aluminum oxide template. Materials Letters 2007; 62(2) 246-248.
26. Ge J, Li Y. Controllable CVD route to CoS and MnS single-crystal nanowires. Chemical Communications 2003; 2498-2499.
27. Zheng Y, Cheng Y, Wang Y, Zhou L, Bao F, Jia C. Metastable γ-MnS Hierarchical Architectures: Synthesis, Characterization, and Growth Mechanism. Journal of Physical Chemistry B 2006; 110(16) 8284-8288.
28. Shen G, Bando Y, Golberg D. Carbon-Coated Single-Crystalline Zinc Sulfide Nanowires. Journal of Physical Chemistry B 2006; 110(42) 20777-20780.
29. Wang Z, Guo R, Li G, Ding L, Ou Y, Tong Y. Controllable synthesis of ZnO-based core/shell nanorods and core/shell nanotubes. RSC Advances 2011; 1 48-51.
30. Jeong N, Cha M, Park YC, Lee KM, Lee JH, Park BC, et al. Single-crystal apatite nanowires sheathed in graphitic shells: synthesis, characterization, and application. ACS Nano 2013; 7(7) 5711-5723.
31. Jeong N, Yeo J. Selective synthesis and superconductivity of In–Sn intermetallic nanowires sheathed in carbon nanotubes. Nanotechnology 2012; 23(28) 285604.
32. Kwiat M, Cohen S, Pevzner A, Patolsky F. Large-scale ordered 1D-nanomaterials arrays: Assembly or not?. Nanotoday 2013; 8(6) 677-694.
33. Hobbs RG, Petkov N, Holmes JD. Semiconductor Nanowire Fabrication by Bottom-Up and Top-Down Paradigms. Chemistry of Materials 2012; 24(11) 1975-1991.
34. Long Y-Z, Yu M, Sun B, Gu C-Z, Fan Z. Recent advances in large-scale assembly of semiconducting inorganic nanowires and nanofibers for electronics, sensors and photovoltaics. Chemical Society Reviews 2012; 41(12) 4560-4580, and references therein.
35. Wagner RS, Ellis WC. Vapor-liquid-solid mechanism of single crystal growth. Applied Physics Letters 1964; 4(5) 89-90.
36. Morales AM, Lieber CM. A Laser Ablation Method for the Synthesis of Crystalline Semiconductor Nanowires. Science 1998; 279(5348) 208-211.
37. Yan X-T, Xu Y. Introduction to Chemical Vapour Deposition. In: Chemical Vapour

Deposition, An Integrated Engineering Design for Advanced Materials. Springer-Verlag London; 2010 p. 1-21.

38. Harker JA. On a new type of electric furnace, with a redetermination of the melting-point of platinum. Proceedings of the Royal Society A 1905; 76(509) 235-250.
39. Ma C, Moore D, Ding Y, Li J, Wang ZL. Nanobelt and nanosaw structures of II-VI semiconductors. International Journal of Nanotechnology 2004; 1(4), 431-451.
40. Wang ZL. Functional oxide nanobelts: Materials, properties and potential applications in nanosystems and biotechnology. Annual Review of Physical Chemistry 2004; 55 159-196.
41. Matsumoto S, Sato Y, Kamo M, Sekata N. Vapor Deposition of Diamond Particles from Methane. Japanese Journal of Applied Physics 1982; 21(4) L183-L185.
42. Beltran-Huarac J. Mn-based nanostructured building blocks: Synthesis, characterization and applications. ProQuest LLC 2014; 3621816 p. 1-182.
43. a) Abrutis A, Silimavicius L, Murauskas T, Saltyte Z, Plausinaitiene V. Doped zinc oxide films grown by hot-wire chemical vapour deposition. Thin Solid Films 2015; 576 89-97.
    b) Abrutis A, Silimavicius L, Kubilius V, Murauskas T, Saltyte Z, Saltyte Z, Kuprenaite S, Plausinaitiene V. On the possibility to grow zinc oxide-based transparent conducting oxide films by hot-wire chemical vapor deposition. Journal of Vacuum Science & Technology A 2014; 32(2) 020602.
44. Prusseit W. Methods of HTS deposition: Thermal evaporation. In: Goyal A (ed) Second-generation HTS conductors. Springer US; 2005. p. 81-96.
45. Lalena JN, Cleary DA, Carpenter EE, Dean NF. Solid-vapor reactions. In: Inorganic materials synthesis and fabrication. John Wiley & Sons New Jersey; 2010 p. 105-140.
46. Choi H-J. Vapor-liquid-solid growth of semiconductor nanowires. In: Yi G-C (ed) Semiconductor Nanostructures for optoelectronic devices. Springer-Verlag Berlin; 2012. p. 1-35.
47. Fan HJ, Lee W, Hauschild R, Alexe M, Rhun GL, Scholz R, Dadgar A, Nielsch K, Kalt H, Krost A, Zacharias M, Gösele U. Template-assisted large-scale ordered arrays of ZnO pillars for optical and piezoelectric applications. Small 2006; 2(4) 561-568.
48. Liu Z, Ma R, Ebina Y, Takada K, Sasaki T. Synthesis and delamination of layered manganese oxide nanobelts. Chemistry of Materials 2007; 19(26) 6504-6512.
49. Rui X, Tan H, Yan Q. Nanostructured metal sulfides for energy storage. Nanoscale 2014; 6 9889-9924.
50. Wang ZL, Kong XY, Zuo JM. Induced growth of asymmetric nanocantilever arrays on polar surfaces. Physical Review Letters 2003; 91(18) 185502.
51. Ma C, Ding Y, Moore D, Wang X, Wang ZL. Single-crystal CdSe nanosaws. Journal of American Chemical Society 2004; 126(3) 708-709.
52. Fang X, Bando Y, Liao M, Gautam UK, Zhi C, Dierre B, Liu B, Zhai T, Sekiguchi T, Koide Y, Golberg D. Single-crystalline ZnS nanobelts as ultraviolet-light sensors. Advanced Materials 2009; 21(20) 2034-2039.
53. Fang X, Bando Y, Liao M, Zhai T, Gautam UK, Li L, Koide Y, Golberg D. An efficient way to assemble ZnS nanobelts as ultraviolet-light sensors with enhanced photocurrent and

stability. Advanced Functional Materials 2010; 20(3) 500-508.

54. Ma C, Moore D, Li J, Wang ZL. Nanobelts, nanocombs, and nanowindmills of wurtzite ZnS. Advanced Materials 2003; 15(3) 228-231.
55. Wang Z, Daemen LL, Zhao Y, Zha CS, Downs RT, Wang X, Wang ZL, Hemley RJ. Morphology-tuned wurtzite-type ZnS nanobelts. Nature Materials 2005; 4 922-927.
56. Dhanam M, Kavitha B, Shanmugapriya M. Structural analysis of CBD γ-MnS thin films. Chalcogenide Letters 2009; 6(10) 541-547.
57. Kim DS, Lee JY, Na CW, Yoon SW, Kim SY, Park J. Synthesis and photoluminescence of Cd-doped MnS nanowires. Journal of Physical Chemistry 2006; 110(37) 18262-18266.
58. An C, Tang K, Liu X, Li F, Zhou G, Qian Y. Hydrothermal preparation of α-MnS nanorods from elements. Journal of Crystal Growth 2003; 252(4) 575-580.
59. Huffman DR, Wild RL. Optical Properties of α–MnS. Physical Review 1967; 156(3) 989.
60. Mochizuki S, Takayama NJ. Spin-wave-assisted photoluminescence in MnS at low temperatures. Journal of Physics: Condensed Matter 1991; 3(16) 2729.
61. Yang P, Lu M, Song C, Gu F, Liu S, Xu D, Yuan D, Cheng X. Luminescence of CaS and MnS nanocrystallites co-activated sol‐gel derived silica xerogel. Journal of Non-Crystalline Solids 2002; 311(1) 99-103.
62. Goede O, Backs W, Hemibrodt, Kanis H. EPR Study of the Antiferromagnetic Phase Transition in (Cd, Mn)S. Physica Status Solidi B 1989; 101(1) 311-318.
63. Audoit G, Mhuircheartaigh EN, Lipson SM, Morris MA, Blau WJ, Holmes JD. Strain induced photoluminescence from silicon and germanium nanowire arrays. Journal of Materials Chemistry 2005; 15 4809-4815.
64. Moloto N, Coville NJ, Ray SS, Moloto MJ. Morphological and optical properties of MnS/polyvinylcarbazole hybrid composites. Physics B 2009; 404(22) 4461-4465.
65. Banewicz JJ, Lindsay R. Magnetic Susceptibility of α-MnS. Physical Reviews 1956; 104(2) 318-320.
66. Kosai K, Fitzpatrick BT, Grimmeiss HG, Bhargava RN, Neumak GF. Shallow acceptors and *p*-type ZnSe. Applied Physics Letters 1979; 35(2) 194.
67. Ye C, Fang M, Zhang L. Temperature-dependent photoluminescence from elemental sulfur species on ZnS nanobelts. Journal of Applied Physics 2006; 99 063504.